CHALMERS
UNIVERSITY OF TECHNOLOGY

Cochlear®

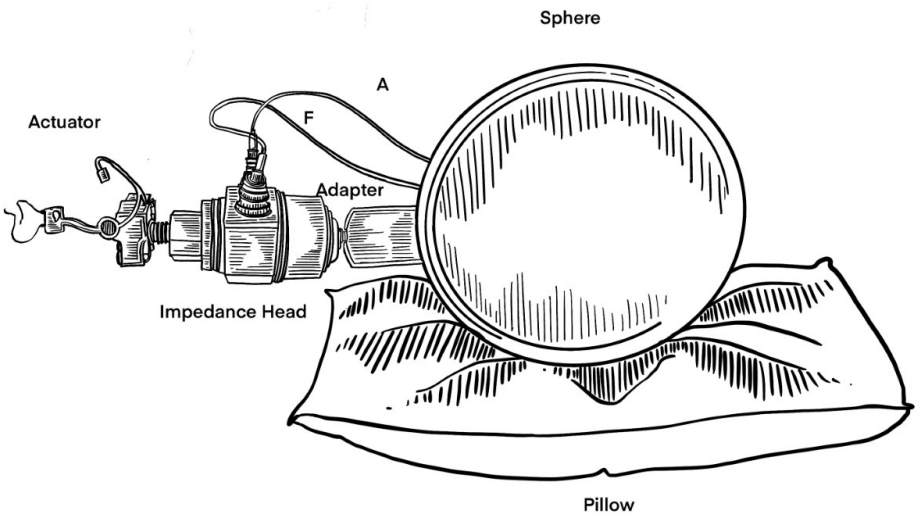

A Pilot Study on Developing an Artificial Head for Bone Conduction Devices Testing Purposes

Master's Thesis in Biomedical Engineering

ASHWIN KUMAAR MURALI DHARAN

Department of Electrical Engineering
CHALMERS UNIVERSITY OF TECHNOLOGY
Gothenburg, Sweden 2021

Master's thesis 2021:EENX30

A Pilot Study on Developing an Artificial Head for Bone Conduction Devices Testing Purposes

Thesis work for Department of Electrical Engineering together with Cochlear Bone Anchored Solutions AB

ASHWIN KUMAAR MURALI DHARAN

CHALMERS
UNIVERSITY OF TECHNOLOGY

Department of Electrical Engineering
Chalmers University of Technology
SE-412 96 Gothenburg, Sweden 2021
Telephone +46 31 772 1000

A Pilot Study on Developing an Artificial Head for Bone Conduction Devices Testing Purposes

ASHWIN KUMAAR MURALI DHARAN

Supervisor: Henrik Fyrlund, Cochlear Bone Anchored Solutions AB
Examiner: Sabine Reinfeldt, Department of Electrical Engineering, Chalmers University of Technology

Master's Thesis 2021:EENX30
Department of Electrical Engineering
Division of Signal Processing and Biomedical Engineering
Chalmers University of Technology
SE-412 96 Gothenburg
Telephone +46 31 772 1000

Cover: Artificial Head Prototype.

Typeset in LaTeX
Printed by Chalmers Reproservice
Gothenburg, Sweden 2021

Pilot Study on Developing an Artificial Head for Bone Conduction Device Testing Purposes

ASHWIN KUMAAR MURALI DHARAN
Department of Electrical Engineering
Chalmers University of Technology

Abstract

Hearing loss is a major health issue throughout the world and reduces the quality of life for people. Various types of hearing implants have been developed to support people with such an impairment. One such type of hearing aid is the bone conduction hearing implants, which facilitate sound transmission to the inner ear via the skull bone, thereby bypassing the outer and middle ears. They are intended for patients with the conductive hearing loss (problems with outer or middle ear), mixed hearing loss (combination of conductive loss and sensorineural loss in cochlea or auditory nerve) and single sided deafness (loss of hearing perception in one of the ears).

For research and development purposes in the bone conduction business, there are some subjective measurements involving human subjects for parameters such as mechanical point impedance, transcranial attenuation, skin attenuation and acoustic feedback. These parameter values are relevant during testing, calibration, product development and quality control phases for bone conduction hearing implants. However, involving human subjects for testing is a challenge, as these are patients, who are surgically implanted with hearing implants, which makes the whole process impractical and cumbersome on a long term basis. Hence there exists a need to develop an alternative, which is the objective measurements of the above mentioned parameters. One option among the objective measurements could be testing on cadavers or post-mortem human surrogates. However, these options have their own pitfalls, in the sense that they change in nature after death, leading to variability in results and there are also ethical issues, which makes this an undesirable option. We could accomplish these objective measurements through development of an artificial or synthetic head, which can illicit the same or similar mechanical and acoustic response as a live human subject would.

This thesis work, which was done in collaboration with Cochlear Bone Anchored Solutions AB (CBAS), focuses on building an artificial head prototype (which consists of an artificial skull, skin and brain assembled together) to be used for testing the bone conduction hearing implants developed by Cochlear. An extensive literature study was conducted to identify materials which could mimic the mechanical properties of the skull, the skin and the brain. These materials/prototypes have been sourced from various facilities throughout the world and they are assembled at CBAS, Mölnlycke, Sweden.

Different brain surrogate materials on spheres were tested and the spheres mechanical point impedance were measured. The obtained results were plotted, compared with the clinical reference and an existing artificial head values. From the results, Permagel was identified as the most suitable brain surrogate material from the test results, which is to be later used on an anatomically correct artificial head for testing all the relevant parameters mentioned before.

Keywords: baha, mechanical point impedance, transcranial attenuation, acoustic feedback, sphere, prototype, artificial head, bone conduction hearing aid, objective measurement .

Acknowledgements

To begin with, I would like to thank my parents, for giving me the opportunity to pursue my higher education in Sweden, for being a constant source of mental support, motivation and also to support me financially throughout my time here in Sweden. Next, I would like to thank my supervisor, Mr. Henrik Fyrlund and his colleagues, namely Mr. Armin Azhirnian, at Cochlear Bone Anchored Solutions AB, for trusting me with this thesis topic, constantly supporting me throughout the thesis work and also the permission to use Cochlear lab facilities, despite the concerns with the ongoing pandemic.

I would like to mention my examiner, Dr. Sabine Reinfeldt for her constant guidance and for being considerate about the delays with my thesis project due to the Corona pandemic. I would also like to thank Dr. Bo Håkansson, for being very patient on the call and answering all my questions including some basic questions. A big thanks and shout out to all the researchers, company representatives who attended calls and collaborated with me for the successful accomplishment of this project. Finally, I would like to thank and acknowledge my friends and room mates, Tejas and Rengaraj for being understanding and considerate throughout the duration of this thesis. Without your constant support, this thesis would not have been possible.

Ashwin Kumaar Murali Dharan, Gothenburg, April 2021

Contents

List of Figures **xv**

Acronyms **xvii**

1 Introduction **1**
1.1 Aim . . . 1
1.2 Objective . . . 1
1.3 Limitations . . . 1
1.4 Scope and Need . . . 2
1.5 Relevant Research Articles and Literature Review Directions . . . 3

2 Background and Theory **5**
2.1 Anatomy and Physiology of human ear . . . 5
2.2 Hearing defects . . . 6
2.3 Anatomy and Physiology of Human Skull, Brain, Skin . . . 7
2.3.1 Skull . . . 7
2.3.2 Skin . . . 8
2.3.3 Brain . . . 10
2.4 Air Conduction and Bone Conduction hearing aids . . . 12
2.4.1 Air and Bone Conduction Hearing . . . 12
2.4.2 Skin Drive . . . 14
2.4.3 Direct Drive . . . 15
2.4.4 BCI . . . 17
2.4.5 In The Mouth . . . 18
2.5 Existing Testing Systems . . . 19
2.5.1 Artificial Mastoid . . . 19
2.5.2 Skull Simulator . . . 20
2.5.3 Head Simulator . . . 21
2.6 Parameters . . . 21
2.6.1 Mechanical Point Impedance . . . 21
2.6.2 Transcranial Attenuation . . . 21
2.6.3 Acoustic Feedback . . . 22
2.7 Existing Studies on Parameters . . . 22
2.7.1 Mechanical Point Impedance . . . 22
2.7.2 Transcranial Attenuation . . . 23
2.7.3 Acoustic Feedback . . . 25
2.8 Simulation Studies . . . 26
2.9 Existing Studies on Material Selection . . . 28

2.9.1 Skull . . . 28
2.9.2 Brain . . . 29
2.9.3 Skin . . . 30

3 Materials and Methods 31
3.1 Materials Selection . . . 31
3.1.1 Skull Surrogate . . . 31
3.1.2 Brain Surrogate . . . 31
3.1.3 Skin Surrogate . . . 32
3.2 Manufacturing Methodology . . . 32
3.2.1 Artificial Skull . . . 32
3.2.2 Artificial Brain . . . 33
3.3 Testing Methodology . . . 35
3.3.1 Mechanical Point Impedance Measurement . . . 35
3.3.1.1 Calibration . . . 37
3.3.1.2 Mass Compensation . . . 37
3.3.1.3 Impedance Measurement . . . 38

4 Results 39
4.1 Sphere 1 - Synthetic Gelatin . . . 39
4.1.1 Impedance Magnitude . . . 39
4.1.2 Phase Measurement . . . 40
4.2 Sphere 2 - Smooth On FlexFoam - iT™ 14 . . . 41
4.2.1 Impedance Magnitude . . . 41
4.2.2 Phase Measurement . . . 42
4.3 Sphere 3 - Smooth On FlexFoam - iT™ 6 . . . 43
4.3.1 Impedance Magnitude . . . 43
4.3.2 Phase Measurement . . . 45
4.4 Sphere 4 - Smooth On FlexFoam iT III™ . . . 46
4.4.1 Impedance Magnitude . . . 46
4.4.2 Phase Measurement . . . 47
4.5 Sphere 5 - Hollow Sphere . . . 48
4.5.1 Impedance Magnitude . . . 48
4.5.2 Phase Measurement . . . 49
4.6 Sphere 6 - Permagel . . . 50
4.6.1 Impedance Magnitude . . . 50
4.6.2 Phase Measurement . . . 52
4.7 Harald . . . 53
4.7.1 Impedance Magnitude . . . 53
4.7.2 Phase Measurement . . . 54

5 Discussion 55
5.1 Final Result . . . 57
5.1.1 Impedance Magnitude . . . 57
5.1.2 Phase Measurement . . . 59
5.2 Comparison of Permagel Head with Dry Skull, Head, FEM . . . 60

6 Conclusion 63

7 Future Work **65**

References **67**

List of Figures

1.1 Discrepancy of skull simulator with head simulator and clinical reference in terms of MPI . . . 2

2.1 Anatomy of human ear. [9] . . . 6
2.2 Anatomy of the skull. [12] . . . 8
2.3 Anatomy of the skin. [16] . . . 9
2.4 Anatomy of the brain. [18] . . . 11
2.5 Air and bone conduction. [20] . . . 13
2.6 Hearing pathways. [21] . . . 13
2.7 Classification of bone conduction hearing devices. [22] . . . 13
2.8 Illustration of skin drive devices. [23] . . . 14
2.9 Illustration of direct drive devices - BAHA. [23] . . . 15
2.10 Cochlear's Baha series of implants. [27] . . . 16
2.11 Surgical implantation of BAHA at mastoid position. [28] . . . 16
2.12 Active transcutaneous BCI with its implantation and external units. [8] . 17
2.13 Illustration of direct drive devices - BCI. [23] . . . 18
2.14 Illustration of the functioning of in the mouth hearing devices. [23] . . . 18
2.15 An artificial mastoid. [37] . . . 19
2.16 TU1000 Skull Simulator. [39] . . . 20
2.17 TU1000 skull simulator with commercially available skull simulators SKS10 and Verifit, respectively. [36] . . . 20
2.18 Schematic illustration of AF path. [46] . . . 22
2.19 Various components of whole head Finite Element model - LiUhead (A-D). [56] . . . 27

3.1 Synthetic gelatin from Humimic Inc. [72] . . . 33
3.2 PUR foams from Smooth On Inc. [73] . . . 34
3.3 Permagel from Forensics Source. [74] . . . 34
3.4 Calibration setup using a laser doppler vibrometer and known weights . . 36
3.5 An impedance head with force and acceleration sensors. . . . 36
3.6 MPI measurement setup with balanced electromagnetic transducer or actuator, impedance head with force and acceleration outputs, connector, sphere to be tested supported on a pillow for decoupling . . . 37

4.1 Impedance plot for Sphere 1 - inorganic gelatin. . . . 40
4.2 Phase plot for sphere 1 - synthetic gelatin. . . . 40
4.3 Impedance plot for sphere 2 - Smooth On FlexFoam - iT™ 14. . . . 42
4.4 Phase plot for sphere 2 - Smooth On FlexFoam - iT™ 14. . . . 43
4.5 Impedance plot for sphere 3 - Smooth On FlexFoam - iT™ 6. . . . 44

4.6 Phase plot for sphere 3 - Smooth On FlexFoam - iT™ 6. 45
4.7 Impedance plot for sphere 4 - Smooth On FlexFoam iT™ III. 47
4.8 Phase plot for sphere 4 - Smooth On FlexFoam iT™ III 48
4.9 Impedance plot for sphere 5 - Hollow Sphere. 49
4.10 Phase plot for sphere 5 - Hollow sphere. 50
4.11 Impedance plot for sphere 6 - Permagel. 51
4.12 Phase plot for sphere 6 - Permagel. 52
4.13 Impedance plot of Harald. 53
4.14 Phase plot of Harald. 54

5.1 Illustration of impedance response of skulls at below, at and above anti-resonant frequency ≈ 150 Hz. [36] 56
5.2 Final Magnitude Plot. 58
5.3 Final Phase Plot. 59
5.4 Comparison of Permagel head with dry skull, head, FEM. [75][55][76] . . 61

List of Abbreviations

ABS	Acetonitrile Butadiene Styrene
AC	Air Conduction
AF	Acoustic Feedback
AFC	Adaptive Feedback Cancellation
AM	Artificial Mastoid
AM	Additive Manufacturing
BAHA	Bone Anchored Hearing Aids
BAHS	Bone Anchored Hearing System
BAI	Bone Anchored Implants
BC	Bone Conduction
BCD	Bone Conduction Devices
BCHA	Bone Conduction Hearing Aid
BCI	Bone Conduction Implant
BEST	Balanced Electromagnetic Separation Transducer
BTE	Behind The Ear
CBAS	Cochlear Bone Anchored Solutions AB
CH	Composite Hydrogel
CM	Contact Mini
CR	Clinicial Reference
CSF	Cerebro Spinal Fluid
DFS	Digital Feedback Suppression
ER	Epoxy Resin
etc	Et Cetera
FEM	Finite Element Model
FFER	Fiber Filled Epoxy Resin
FIR	Finite Impulse Response
FMJMSC	Full Metal Jacket Mild Steel Core
ITE	In The Ear
LDV	Laser Doppler Vibrometry
MCH	Modified Composite Hydrogel
MPI	Mechanical Point Impedance
MRI	Magnetic Resonance Imaging

N	Newton
PBS	Phosphate Buffered Saline
PDMS	Polydimethyl Siloxane
PETG	PolyethyleneTerephthalate Glycol Modified
PLA	Poly Lactic Acid
PMHS	Post Mortem Human Surrogates
PTA	Pure Tone Average
PUR	Polyurethane
PVA	Poly Vinyl Alcohol
SIN	Speech In Noise
SLA	Stereolithography
SSD	Single Sided Deafness
TA	Transcranial Attenuation
TBI	Traumatic Brain Injury
TM	Tymphanic Membrane

1
Introduction

1.1 Aim

The primary objective of this thesis is to develop an artificial head consisting of a sphere and brain surrogate material, which could reliably mimic the mechanical properties of the human head. This head is then measured for its mechanical point impedance (MPI) values and compared with clinical reference (CR) values. Suitable brain surrogate material is to be identified based on the outcome of these tests, and this material could later be used in an anatomically correct artificial head.

The aim is to develop this solution as an alternative to live human testing dependency bottleneck and also the well-documented issues with cadavers and Post-Mortem Human Surrogates (PMHS), giving varying results with time as it degrades and also the associated ethical issues with the same. To summarize, an attempt has been made to develop a novel objective measurement alternative to subjective measurements involving live human subjects. The end goal is to develop a head prototype with an embedded accelerometer, specifically tailored for bone conduction implant testing purposes.

1.2 Objective

To begin with, an exhaustive literature study was conducted to understand the task at hand and to accelerate the process. Relevant scientific articles were researched for identifying suitable surrogate materials for the skull, skin, and brain. This quest further involved interviews and consultations with relevant researchers and companies. Based on extrapolation from similar studies with different applications, materials that could be suitable for this application were shortlisted. Identified materials and prototypes were procured from specialist skull manufacturing and materials manufacturing companies throughout the world. Finally, the artificial head was cast/assembled at Cochlear facilities for mechanical testing.

1.3 Limitations

The main limitation of this study were that not many relevant head phantoms have been developed for testing bone conduction devices (BCD) and hence limited information was available from scientific studies. Certain materials were identified to mimic the mechanical properties of the human brain like composite hydrogel (CH), agar/beef powder-based

gelatin. However, since they are organic and contain water, they are unstable in the long term. Hence the viable choices of brain phantom materials drastically reduced in number.

1.4 Scope and Need

There are few existing artificial heads at Cochlear, also called the head simulator, which is spheres consisting of filler material and an artificial skin on top. The filler material suffers from microbial contamination and degradation with time, leading to variability in results. The need of this project is to identify synthetic brain surrogates, which do not suffer from the issues mentioned above, must give reliable and repeatable results in terms of mimicking the mechanical and acoustic properties of the human head. The skull simulator, which is the current industry standard, has a completely different mechanical impedance in comparison to the CR values and even the mechanical impedance obtained from the head simulator as shown in Figure 1.1. From the brain surrogate identified through this thesis work, the future plan is to test it on an anatomically correct skull and try to match the impedance response with that of CR.

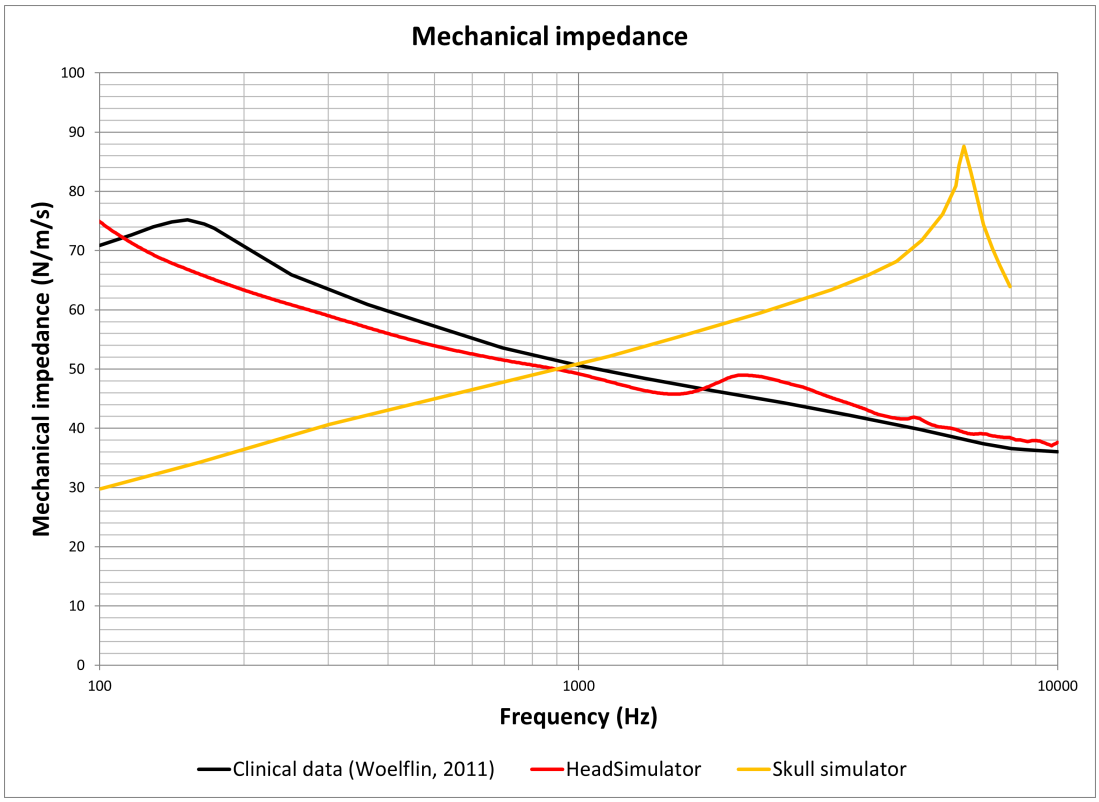

Figure 1.1: Discrepancy of skull simulator with head simulator and clinical reference in terms of MPI

1.5 Relevant Research Articles and Literature Review Directions

There are some existing skin-skull-brain models, which have been developed and studied in the literature, albeit for varying applications, namely for defense purposes like the impact of blast waves on the human head, assessment of gunshot impact through the head, analysis of traumatic brain injury (TBI). Through these studies, useful information was extrapolated, even though they did not have a straightforward and direct correlation to the prototype.

Freitas et al [1], developed a human head surrogate model with embedded sensors to measure the behind helmet blunt trauma injuries. This model was able to achieve a balance between biofidelity and ease of use. Mahoney et al. [2], developed a skull-brain model to investigate the fracture pattern when the developed synthetic head was subject to steel bullet shots. The entry and exit patterns of the bullet in head were analyzed by assessors and marked based on closeness to reality. In a successive study, again Mahoney et al. [3], developed a skin-skull-brain synthetic head that was subjected to Full Metal Jacket Mild Steel Core (FMJ MSC) bullets, and the impact developments were captured by a high-speed camera and computed tomography. Various parameters like entry and exit wounds, fracture patterns, and wound tracts were analyzed by experienced forensic pathologists, radiologists and these were graded on a Likert-type scale.

Sutar et al. [4], developed a 1D Finite Element Model (FEM) of human head surrogates to investigate the blast-induced TBI. Through this study, they were able to understand the blast wave propagation through the layered architecture of the human head. They also inferred the amplification provided by the skin and meninges as well as the attenuating property of air sinuses among the other results. Thali et al. [5], developed a skin-skull-brain model to reliably reconstruct and reproduce blunt force head injury on the surrogate model in a laboratory environment. The results compared favorably to a real human head subjected to an equivalent load or impact. Again, Thali et al. [6], used the same "skin-skull-brain" model to investigate the gunshot wound effect on the head, even though it was one of the earliest studies of its kind. It was the first skull model developed which could mimic the three-layer structure of human skulls - outer tables-diploe-inner tables.

2

Background and Theory

2.1 Anatomy and Physiology of human ear

The human ear could be broadly divided into three categories - the external ear, middle ear, and the inner ear, as shown in the Figure 2.1. The outer ridged flap-like structure is called the pinna, which directs the sound waves towards the ear canal or the external auditory meatus [7]. This ear canal is about 2.5 cm in length. This region is roughly made up of one-thirds of cartilage and two-third of bone. The ear canal leads up to TM which can vibrate under the influence of sound waves. The external ear directs the external sound waves. It also amplifies the mid-frequencies of the sound waves, so that we could get a sense of the direction of the incoming sound wave [8]. The ear canal also secretes a sticky substance called cerumen or ear wax, which traps dirt and it is also partly anti microbial.

The middle ear comprises the TM, which is an air-filled cavity. It has three ear ossicles - malleus (hammer), incus (anvil), stapes (stirrup). The Malleus is attached to the TM and pulls it inward, leading to its conical shape. Attached to the oval window are the stapes. The round window is located next to the oval window. The Eustachian Tube originates in the middle ear and connects to the nasopharynx region. This tube balances the pressure difference between the middle ear and external atmospheric pressure, especially when a person is chewing or yawning [7]. This is the region, where the acoustic sound wave is being converted to mechanical vibrations and passed onto the inner ear through the stapes in contact with the oval window [8].

There are three main constituents of the inner ear - the three semi-circular canals, the vestibule, and the snail-shaped Cochlea. The cochlea is responsible for the hearing sensation while the vestibular regions and semi-circular canals are responsible for equilibrium and balance. The inner ear comprises the bony labyrinth and membranous labyrinth, wherein the membranous labyrinth lies inside the bony labyrinth. The cochlea consists of three tubes that are arranged together as a snail shell [7]. Scala Tympani is the top layer that originates from the oval window and Scala Vestibuli is the bottom layer which ends in a round window. Both these layers are filled with a liquid called Perilymph, which is rich in Sodium and has a lower concentration of Potassium. The middle region is called Scala Media, also called Cochlear Duct. This region is filled with Endolymph, which has a lower concentration of Sodium and a higher concentration of Potassium. The layer separating the Scala Vestibuli and Cochlear Duct is known as the vestibular membrane. The layer which separates Scala Tympani and Cochlear duct are known as Basilar Membrane [8].

Organ of Corti is present in this region and is lined with hair cells. The sound stimulates these hair cells and an action potential is generated, leading to an electrical signal, which is passed onto the auditory nerve for further interpretation by the brain [7].

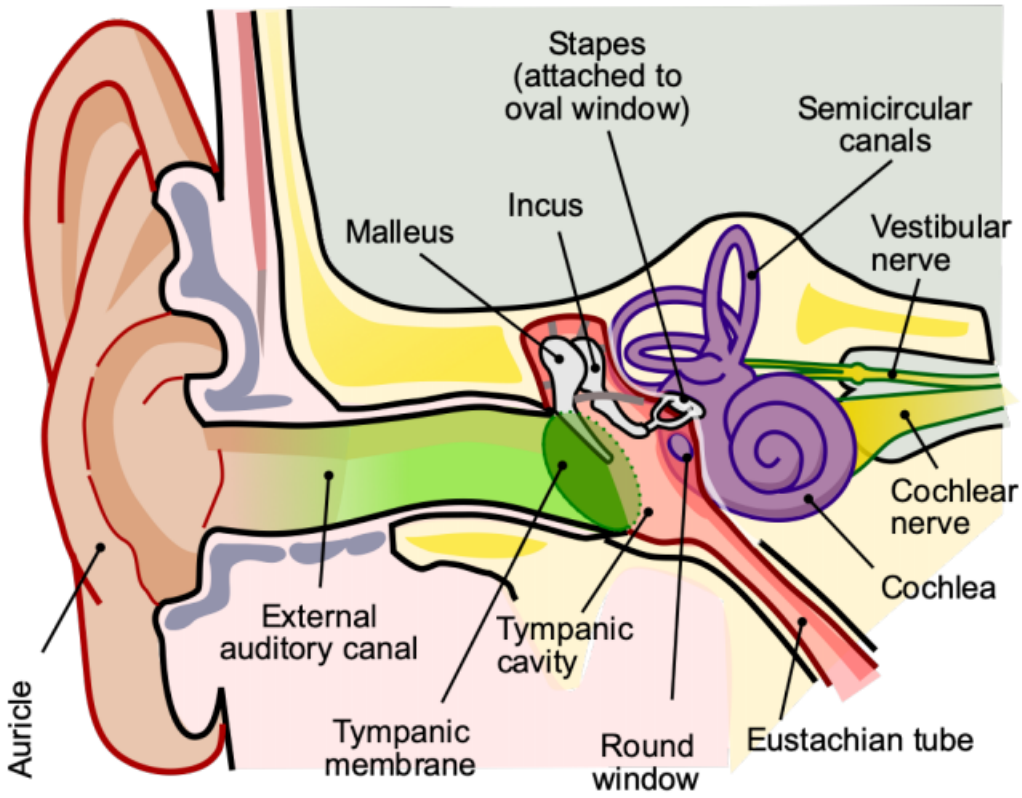

Figure 2.1: Anatomy of human ear. [9]

2.2 Hearing defects

Hearing defects or losses can be either reduced hearing sensation and perception or a complete lack of hearing sensation and perception. A patient can either be born with this disorder or acquires it during a certain point in their lifetime. Reasons behind these losses could be either environmental or even biological. These defects can either be single-sided or dual sides of the ear with varying severity and degrees of damage. Broadly speaking, the hearing defects could be classified into three types: conductive losses, sensorineural losses, mixed losses. In addition, the losses could also be categorized as central, wherein there is damage to the brain stem or the auditory nerve which passes to the brain. Another case is non-organic, where they are no anatomical or physiological damage.

Conductive losses arise due to problems in the outer and middle ear, which does not facilitate the proper acoustic sound propagation into the fluid-filled layers of a properly functioning inner ear and attenuates the incoming acoustic sound waves. These losses are caused due to infection in ear wax (chronic otitis media), deformation of the external auditory meatus (atresia), damage to TM (perforation), stiffening of the three auditory

ossicles, and otosclerosis (Stapes attachment to the oval window) [10]. Mixed loss is a combination of both conductive and sensorineural losses. It is mainly due caused to birth defects such as vestibular Aqueduct syndrome which arises due to abnormal diameter of the region and also due malfunctioning of ear bones [11]. We can use Bone Conducting hearing aids as a measure to combat both these losses.

Sensorineural losses occur due to damage in the brain stem or cochlear hair cells. This damage occurs due to intense and sudden sound exposure, ototoxic chemicals released with antibiotics/drug uptake, allergic reaction, and autoimmune conditions due to the inherent hereditary genes. Another reason for these losses is the malfunction of the hair cells in the organ of corti. This affects the generated electric signal which is to be sent to the brain. Presbyacusis or age-related hearing loss is a sensorineural loss, which causes permanent and irreversible damages on the auditory nerve and brain stem [8]. For cases such as mild sensorineural loss and presbyacusis, we can use air conduction aids, as they can still transmit amplified sound waves to the cochlea. However, for severe sensorineural cases, the best treatment is to employ cochlear implants wherein their electrodes are in direct contact and thereby stimulate the nerve endings of the hearing region.

2.3 Anatomy and Physiology of Human Skull, Brain, Skin

2.3.1 Skull

The anatomy of the human skull is depicted in Figure 2.2. The human skull consists of 22 bones, namely the 14 facial bones and the eight cranial bones, which are connected through joints, resembling a suture and protects our brain [12]. Out of these bones, only mandibular and temporomandibular joints are movable. Two out of these eight cranial bones are pairs and twelve out of these 14 facial bones are pairs. The human skull is made up of three layers: an outer table, spongy energy-absorbing middle layer called diploe, and inner tables. They are anisotropic in nature.

Let's first focus on the cranial bones. Frontal bones occupy the forehead region and also the frontal portion of the skulls, covering the frontal lobe of the brain. The occipital bone occupies the back portion of the head and continues right until the skull base, thereby covering the occipital lobe of the brain. The middle region consists of a pair of bones called parietal bones. Attached towards the sides around the temporal region on both sides are the temporal bones. These temporal bones are primarily involved in hearing and bone conduction (BC) as they also include the mastoid bone and external auditory meatus, both of which have a big role to play in the hearing mechanism. Right between the temporal bone and Zygmoid bone lies a long butterfly-shaped single bone called the Sphenoid bone, which spans the entire width of the skull. Just in front lies the Ethmoid bone, between the Sphenoid and Nasal bones, whose surface is a bit perforated and sieve-like, also called cribriform plates [7].

Now coming to the 14 facial bones, the mandible is a single bone, which represents the lower jaw and is the strongest and longest bone in the face. Another single bone is the

vomer, which is the inferior part of the nasal septum. We have a pair of nasal bones in the upper part of the nasal region. Inside the nasal cavity, there are a pair of bones called inferior nasal concha, wherein the word "concha" signifies the bones being shell-shaped. Right inside the eye cavity is a pair of lacrymal bones, in each eye cavity. The lacrimal fluid refers to the tears of the eye. Fittingly, these bones are located right next to the tear ducts. We also have a pair of cheekbones on either side called the zygomatic bone. The bone which lies beneath the posterior portion of the palette in our mouth represents the palatine bone. Finally, it is the maxilla bone pair, which occupies most of the space in our face. These human skull bones give structure/stability to the head and also protects the brain from direct impact [13][7].

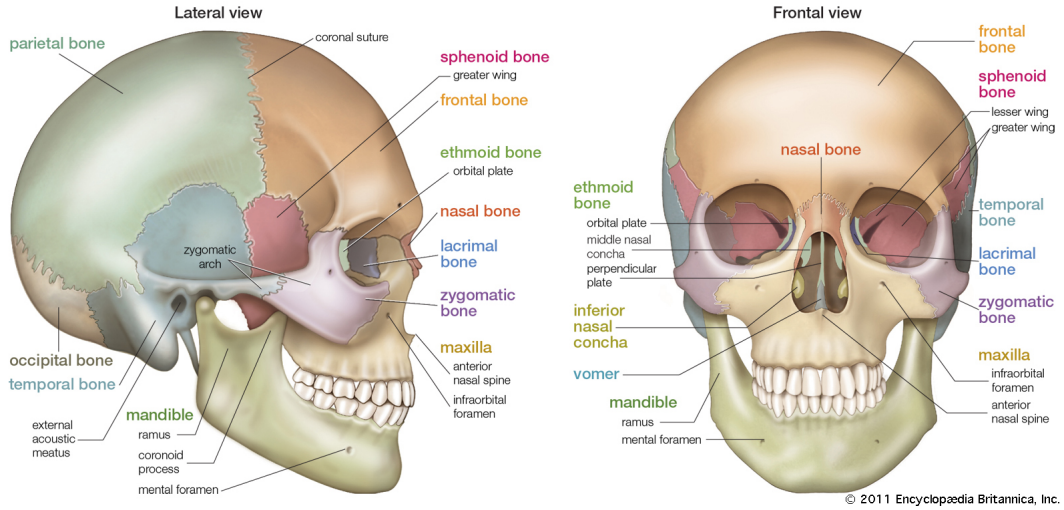

Figure 2.2: Anatomy of the skull. [12]

2.3.2 Skin

Human skin consists of two layers, namely the epidermis and dermis [7] as can be seen from Figure 2.3. Below the dermis lies the hypodermis or subcutaneous tissue, deep fascia, muscles, and bone. Skin is the biggest organ in the human body [14]. The epidermis is the outermost surface of the skin, which acts as a barrier, it is made up of stratified squamous epithelium and keratinocytes. There are typically five layers within the epidermis [14]. Stratum Basale is the cuboidal-shaped bottom-most layer and is supplied with blood from blood capillaries in the dermis. It also has Merkel cells, which are responsible for touch sensation [14]. Stratum Spinosum is the layer on top, which is not supplied with any capillaries, cells begin to divide in this region and move upwards. This region also has some specialized cells such as Melanocytes, which is responsible for skin color pigmentation, and Langerhans cells, which function similarly to white blood cells of the blood, where it handles the foreign body pathogens which enter the skin surface and also other immunological functions. The layer on top is Stratum Granulosum, which consists of flat and elongated keratin cells, which are granulated. Further upward is Stratum Lucidum, which is a layer of dead keratin cells. This layer is predominantly found in the palms and soles of the feet. Finally, up top is the Stratum Corneum layer, which is again dead keratin cells, which one tends to lose quite frequently and are replaced.

The Dermis is a region with connective tissue and composed mainly of collagen and elastin, which secrete extracellular matrix [7]. This region provides flexibility and support. The hair follicle arises here and passes through the epidermis outside. It also has the sebaceous gland, which lubricates the hair. Arrector pili muscle straightens the hair when one is shocked and having a goosebumps moment or even during extremely cold weather conditions [15]. There are eccrine and apocrine sweat glands that produce sweat, for excreting unwanted substances from the body and also for thermal regulation of the body [15]. There are also blood capillaries that start in this region and project up to the base of the epidermis. There are cells in this region called fibroblasts, which secrete extracellular matrix, throughout this region. This region also has the mast cells, which has a crucial part in an allergic reaction, inflation, and hypersensitivity.

The Hypodermis region is primarily composed of a fatty layers of tissues and their main role is insulation [7]. Generally speaking, the main functions of skin include it serving as a physical barrier, vitamin D synthesis, temperature regulation, sensation, prevention of water loss and abrasion, serving as containment for body, and providing structure to the body [15].

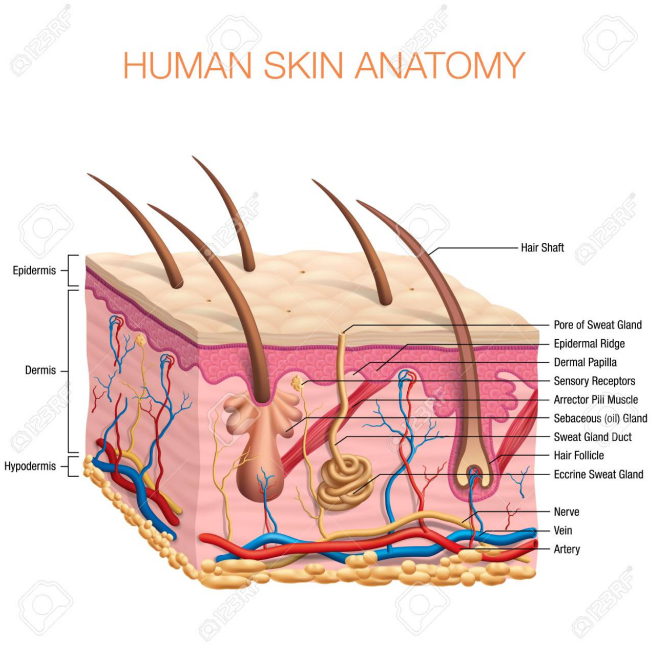

Figure 2.3: Anatomy of the skin. [16]

2.3.3 Brain

The Brain is the controlling center of our body. It is composed of billions of nerve cells [17][7]. The cells which constitute the brain are primarily of two types - Neurons and glial cells. The neurons are responsible for the exchange of nerve impulses. Glial Cells on the other hand helps to maintain homeostasis, produce Myelin, facilitate signal transmission, overall support, and nourishment of the brain [18]. The brain is housed in meninges which include Piamater, Dura mater, Arachnoid matter [17]. A watery substance called Cerebro Spinal Fluid (CSF) surrounds the brain/spinal cord and provides insulation or protection. There are special structures within the ventricles called the Choroid Plexus, which is responsible for CSF production [17][7]. Blood supply to the brain is handled by two arteries - the internal carotid artery which supplies the cerebrum and the vertebral arteries which supply the brain stem, cerebellum, and the bottom part of the cerebrum [17]. The brain communicates with the rest of the body through the spinal cord and twelve pairs of cranial nerves. These cranial nerves control smell, vision, hearing, breathing, movement of the eye, head, and face among other functions.

The brain has three main parts, namely the Cerebrum, Cerebellum, and Brain Stem, as it can be inferred from the anatomy of the brain illustrated in Figure 2.4. The cerebrum is the largest part of the brain and it can be divided into the left and right hemispheres. These left and right hemispheres are connected through the Corpus Callosum [17][7], which facilitates the communication between these two hemispheres. Also, each of these hemispheres controls the other side of the body. The outer surface of the cerebrum has the grey matter, while the inner surface is composed of white matter. The outer surface called Cortex, also has grooves called Sulci and ridges called Gyri, throughout the outer surface [17][7]. This outer surface is typically convoluted. The cerebrum contains regions that are responsible for vision, touch, hearing, speech, motor movement, reasoning, logical thinking, learning, emotions.

The Cerebrum could be divided into four lobes - Frontal, Parietal, Occipital, and Temporal [17][7][18]. The Frontal lobe is the biggest of the four lobes. They are responsible for personality, emotions, behavior, intelligence, decision making, planning, critical thinking, concentration, and self-awareness of the human subject. There is a small region within the frontal lobe called the Broca's area, which controls speech and writing ability [17][18]. There is also the motor strip area within this lobe, which controls the movement within our body. The Parietal lobe region has the sensory strip area which interprets the sense of touch, pain, and temperature. This region also interprets language, speech, hearing, vision, memory, sensory, and motor areas. This region is also responsible for spatial and visual perception. The temporal lobe is found in the temporal bone region and along the side region of the head. This region has the Wernicke's area which can be used to understand language [17][18]. Other main functions include hearing, memory, sequencing, and organization. Finally, the Occipital lobe is present on the backside of the head. This region is primarily focused on interpreting vision based on color, movement, and light.

The cerebellum is located just below the Cerebrum. This region is connected to the brain through a connection with the brain stem. It is responsible for balance, coordination, and maintenance of body posture [17][7][18]. Finally, the spinal cord enters the cranium through a hole in the cranium called the Foramen Magnum [17] and the brain stem forms

the lower part of the brain. The brain stem consists of Medulla Oblongata, Pons, and Mid Brain [7][18]. The "to" and "fro" exchange of information from the cerebral cortex to the spinal cord and vice versa takes place through the pons and brain stem. Damage to this region leads to brain death.The midbrain controls eye movement. The pons is responsible for coordinating eye and facial movement, facial sensation, hearing, and balance. Medulla Oblangata controls breathing, blood pressure, swallowing and heart rhythm. .

There are some other "deep" structures within the brain. Hypothalamus works with the autonomous nervous system. It controls sleep, sexual response, thirst, and hunger. Thalamus acts as the center for the exchange of impulses with the cortex. They have a role in pain sensation, attention, memory, and alertness [17][7][18]. The pituitary gland, also called the "master" gland, controls the endocrine glands and their hormones [17]. These hormones regulate sexual growth, muscle and bone growth, stress response. The pineal gland regulates the body's internal clock and circadian rhythm [17]. The amygdala controls emotional response and hippocampus is responsible for memory [17].

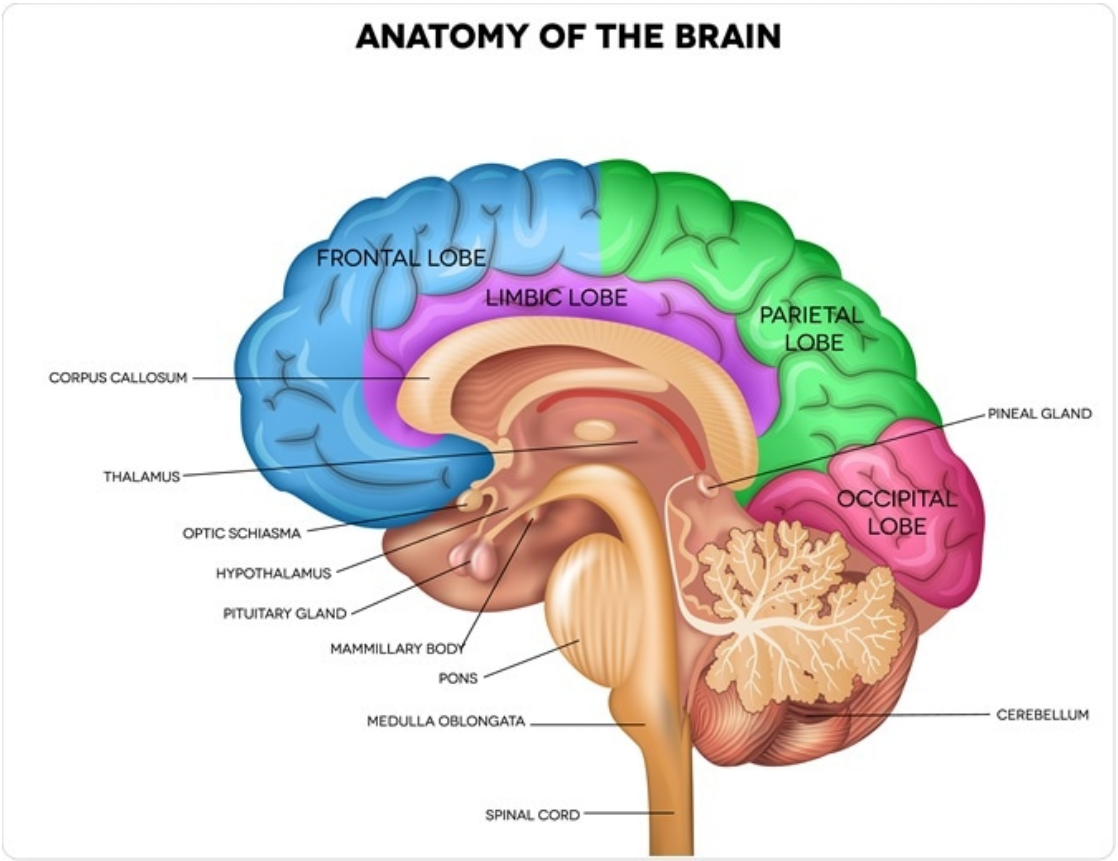

Figure 2.4: Anatomy of the brain. [18]

2.4 Air Conduction and Bone Conduction hearing aids

2.4.1 Air and Bone Conduction Hearing

Air and bone conduction is illustrated in Figure 2.5 for easier understanding. Air conduction (AC) hearing is the normal hearing pathway wherein the acoustic sound waves (longitudinal) enter the auditory canal through pinna and strike the TM to get converted into mechanical vibrations. These vibrations are transferred through the three auditory ossicles to the oval window. These vibrations enter the scala vestibuli and scala tympani regions which are filled with endolymph. Finally, they enter scala media, which is filled with perilymph. These vibrations exert an inertial force on these inner ear fluids [19]. This stimulates the hair cells and cilia on the basilar membrane. Each region is stimulated differently according to the frequency of vibration at that region. This leads to a chemical change at hair cells and cilia, thereby resulting in nerve impulses that are generated and carried to the temporal regions on both sides of the brain. Both these signals are processed and compared, suppressing the noise so that one could localize the sound and hear properly. AC aids are worn externally, usually behind the pinna. It has a microphone that collects sound, processes it, amplifies it to the desired level, and feeds it to the transducer, which is a miniaturized loudspeaker.

BC hearing bypasses the outer and middle ear, the rest of the hearing mechanism is the same as AC, thereby leading to hearing perception. There are two ways by which BC hearing can occur - either through BC transducer, which sums up the surrounding sound waves, or our voice, which passes to the inner ear as vibrations through our teeth, oral cavity, facial bones, and cartilages. There is a difference when we hear our voice live and a recorded version. This is because the recorded version does not include the contribution from BC, only the AC sound is included. Contribution to the BC sound is majorly through the skull bone, but also through the fluids in the head such as CSF, skin, soft tissue, and cartilage. All these structures play their part in vibrations and power transmission in the head. The various hearing pathways are illustrated in Figure 2.6 and one can get a sense of the classification of the BC through Figure 2.7, which shall be covered in detail in the upcoming sections.

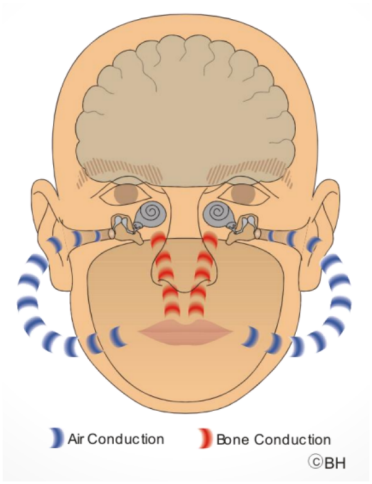

Figure 2.5: Air and bone conduction. [20]

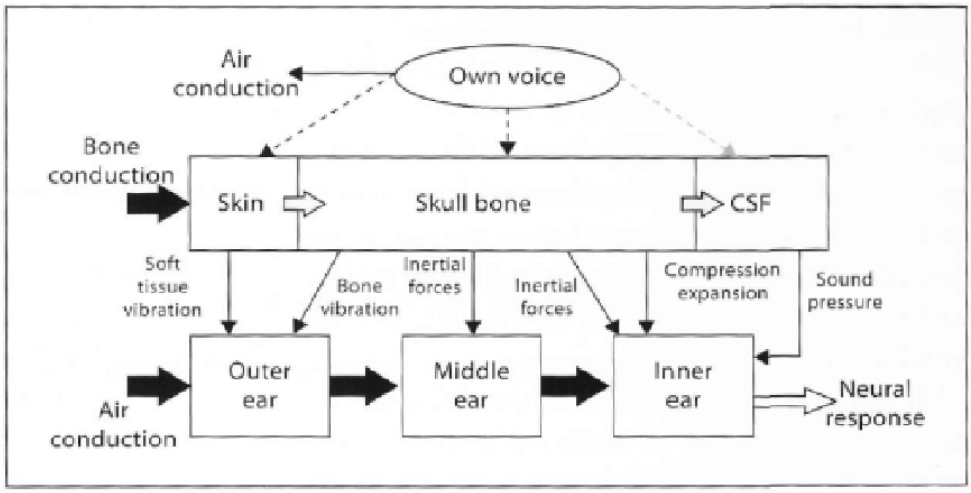

Figure 2.6: Hearing pathways. [21]

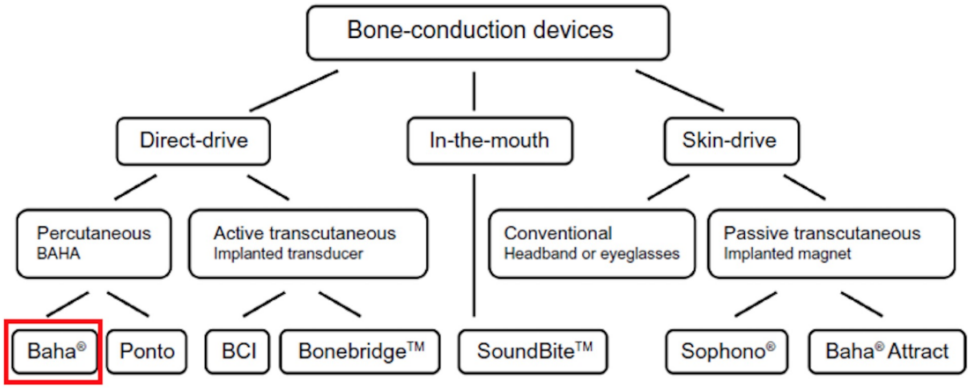

Figure 2.7: Classification of bone conduction hearing devices. [22]

2.4.2 Skin Drive

Skin drive devices are those in which the vibrations generated from the transducer are passed through the skin for BC in the skull, as illustrated in Figure 2.8. There two major classes of skin drive devices - conventional and passive transcutaneous as shown in Figure 2.7 [22]. Conventional devices are completely non-invasive and surgery-free, as they have a microphone, sound processor, and transducer outside and behind the ear, enclosed in a housing and held in place through means such as headband, steel spring, or eyeglasses. To ensure the vibrations are properly transmitted to skull bones, the conventional hearing aid must be pressed against the head with a static force of typically 2N [8]. This might cause pain, irritation, and discomfort after prolonged usage. They also suffer from vibration damping due to skin and subcutaneous tissue, thereby reducing its intensity reaching the cochlea [8]. These devices are easy to use and simple, making them an ideal candidate for children or intellectually disabled patients [8].

Passive transcutaneous devices are the same as conventional BCDs, with the only difference being that a magnet is surgically implanted beneath the skin and this magnet keeps the device in place and does not allow it to move [22]. This will ensure efficient transfer of power and it is an aesthetically appealing solution [22][8]. It also suffers from the static force on the skin issue, where there is dampening provided by the skin over 2 Khz, thereby reducing the electroacoustic function of the aid [8]. Currently available passive transcutaneous devices on the market include sophono and baha attract.

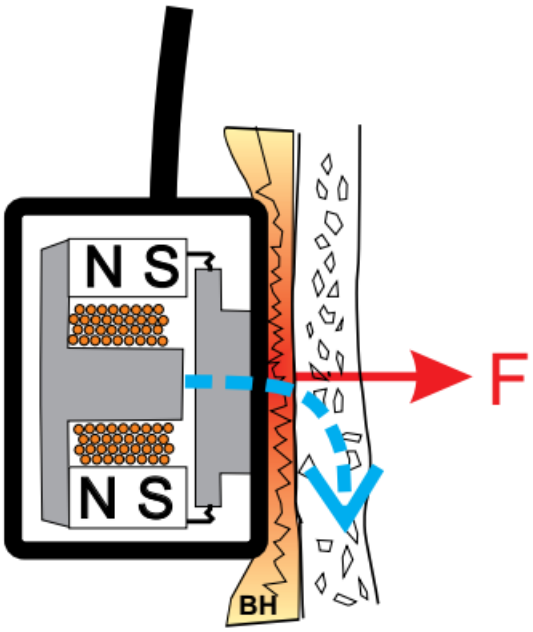

Figure 2.8: Illustration of skin drive devices. [23]

2.4.3 Direct Drive

BCDs, where vibrations are given directly to skull bones, are called direct-drive devices, as it is illustrated in Figure 2.9. These devices can avoid the damping provided by the skin and soft tissues, thereby a stronger intensity signal can be directly stimulated on the skull bone [24]. One such direct BCD is the Baha series from Cochlear BAS, as shown here in Figure 2.10. Another competitive device on the market is the Ponto series from Oticon Medical. This device has titanium implants along with the abutment, implanted directly in the parietal skull bone, thereby creating a permanent skin penetration. This titanium implant osseointegrates typically within three months. An external unit consisting of a microphone, sound processor, transducer, battery, and other electronics is enclosed in a casing and attached to the abutment. The artificial head, which is to be developed through this project, is predominantly to test these devices. Bone Anchored Hearing Aids (BAHA) serves as the gold standard of implantable BCDs used to treat congenital malformations and middle ear defects. It also has an easy and safe surgical implantation procedure, as illustrated here in Figure 2.11, which makes it suitable for a large patient group. Users also report increased wearing comfort and sound quality [25][26]. Some limitations do exist like the potential skin irritation, granulation tissue formation, infection, requirement for daily lifelong care, possibly coming off the head through trauma, aesthetic and social stigma [8].

Another class of direct drive devices is the active transcutaneous devices. There is no permanent penetration of the skin and a transducer is implanted in the skull, thereby facilitating direct bone conduction. They use both implanted and external magnets and transmit signals from the external units via inductive link. They suffer from skin damping, though not at the levels of skin drive devices. An example of this class of device is the Bonebridge series from Medel. They do not suffer from the acoustic feedback problem as the microphone and transducer are separate. However, the surgical procedure to implant transducer and magnets are a bit complicated [8], with Bonebridge being more invasive in comparison to BAHAs. More information about this class of devices will be discussed in the upcoming BCI section.

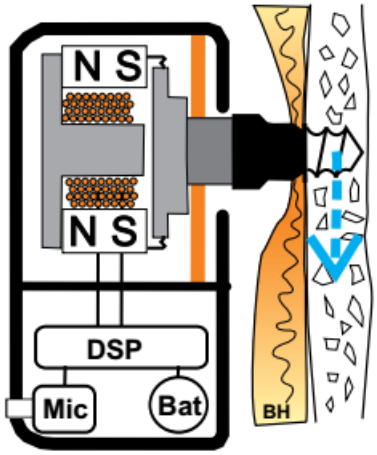

Figure 2.9: Illustration of direct drive devices - BAHA. [23]

Figure 2.10: Cochlear's Baha series of implants. [27]

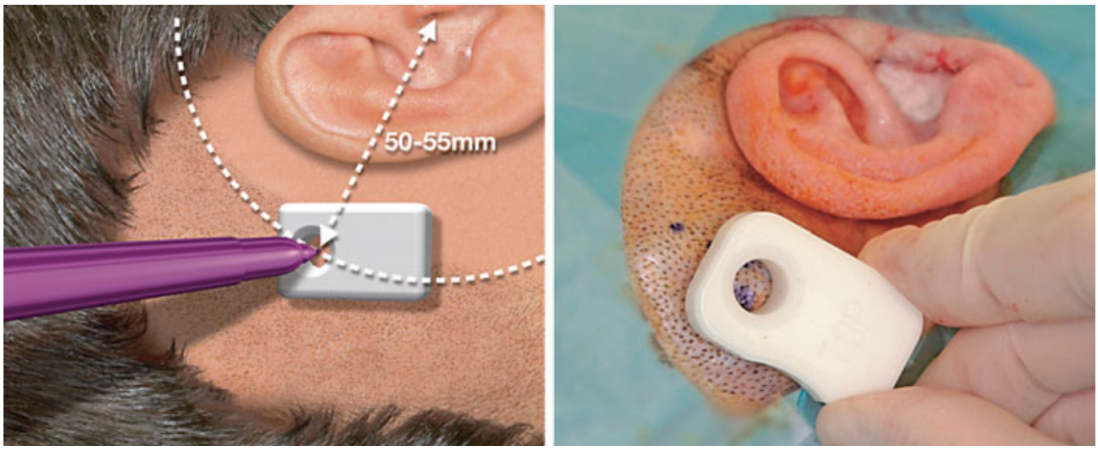

Figure 2.11: Surgical implantation of BAHA at mastoid position. [28]

2.4.4 BCI

Bone Conduction Implants (BCI) is an example of active transcutaneous BCD. BCI, shown in the Figure 2.12 was developed as an alternative to percutaneous BAHA and underwent clinical trials in recent years. This was developed as a joint effort between the Chalmers University of Technology, Sahlgrenska University and the University of Gothenburg [8]. The main advantage of this device is that it leaves the skin intact. It has both an external unit which is magnetically retained in position and implanted unit, which is surgically implanted in the skull at the mastoid bone beneath the skin and soft tissues. The external unit consists of two directional microphones, a battery, a digital signal processor, an external magnet, a modulating circuit, and a transmitting coil, all encased in a plastic housing. The implanted unit consists of an internal holding magnet, receiving coil, demodulating circuit, and a BC transducer. The microphone receives the acoustic signal, it is processed and amplitude modulated before the generated electro-magnetic signal being transmitted through an inductive link to the implanted unit. This signal is received and demodulated before being fed to the BC transducer, which then functions similarly to a direct bone conduction transducer i.e., vibration transmission via skull bones [29]. The transmitted signal must have sufficient power to stimulate the cochlea and create a proper hearing perception. The overall working principle and the vibration transmission to Cochlea are illustrated in Figure 2.13. The BC transducer used here is Balanced Electromagnetic Separation Transducer (BEST), which was invented in 2003 by Dr. Bo Håkansson [30]. This transducer reduces distortion and is compactly designed. This also makes it anatomically more suited to a wider group of patients.

The surgical procedure to implant BCIs were found to be safe, effective and reliable. A previous study investigated the effects of MRI on BCI and found it to be MR conditional when tested under the MRI field of 1.5 Tesla [31][32]. Another issue with the BCI is that the inductively transmitted signal does undergo distortion through the skin of the order 10-15 dB [33][34] even though it is less than the 20dB distortion associated with skin drive devices [22][35]. This issue could be countered by implanting the transducer as close as possible to the cochlea and high-frequency boost experienced by the transducer between 2500 to 6500 Hz to increase its output force [29].

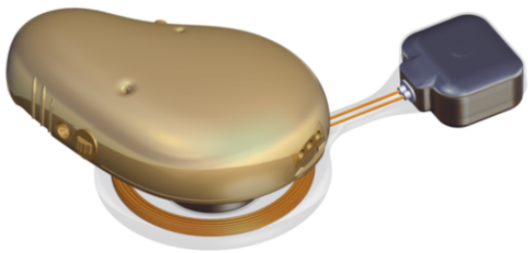

Figure 2.12: Active transcutaneous BCI with its implantation and external units. [8]

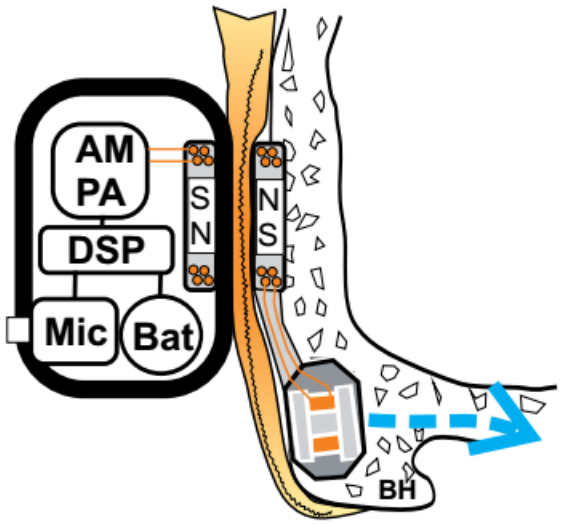

Figure 2.13: Illustration of direct drive devices - BCI. [23]

2.4.5 In The Mouth

An illustration of the functioning of the "In the mouth" devices is shown in Figure 2.14. These devices transmit BC sound owing to a direct and firm connection between the teeth/jaws and the skull bone. A popular example of this type of device is the Soundbite series released by Sonitus medical, which is no longer in the market anymore. Nonetheless, it is still interesting to understand their working principle. A piezoelectric transducer is attached to the upper left or right back teeth. A microphone is attached behind the ear, which transmits the acquired acoustic sound waves wirelessly to the transducer at teeth. This method is completely non-invasive, which is its main advantage. However, the oral environment is acidic, which makes it unsuitable for any electronic component [8]. Also, this device might suffer from problems associated with acoustic feedback, noise disturbance, and discomfort, predominantly while eating. Since the transducer is placed inside the mouth, it needs to be very compact, which reduces the power output. Hence we can say that it is suitable for single-sided deafness (SSD) over a conductive or sensorineural hearing loss. This is because the primary aim is to have a high frequency gain to overcome the head shadow effect and could be designed as a low power-consuming device [23].

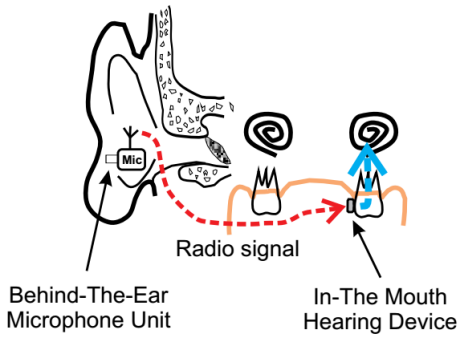

Figure 2.14: Illustration of the functioning of in the mouth hearing devices. [23]

2.5 Existing Testing Systems

2.5.1 Artificial Mastoid

Artificial mastoid (AM) is an artificial load developed for the objective measurement of output force measurements, as shown in Figure 2.15. It represents the load of skin-covered mastoid region alone, which makes it suitable for testing and calibration of transcutaneous BC devices [36].

Figure 2.15: An artificial mastoid. [37]

2.5.2 Skull Simulator

Skull simulator was developed by Dr. Bo Håkansson in 1989 and it is shown in the Figure 2.16. It was a novel system, which substituted/models the skull as a pure mass system. The estimated mass of the skull is 2.5 Kg [36]. Usage of this skull simulator enabled objective measurement of output force measurement. The basic concept behind these devices is that the mechanical impedance of the load, which in our case is the skull simulator should be greater than the mechanical impedance of the transducer. Also, the weight of the load must be at least thrice or more of the weight of the transducer. Only if the above two conditions are satisfied, one can consider it as a constant force source [36], which enables the skull simulator to function as intended. This development played a key role in the development of percutaneous BCDs such as baha or ponto.

The CR values of human subjects were estimated later through a study by Woelflin et al [38]. A discrepancy was noticed when comparing MPI values generated by the skull simulator and the CR. Hence the need existed for developing an alternate solution that could closely mimic the CR. An in-house solution called a head simulator was developed by Henrik Fyrlund at Cochlear BAS, which will be discussed in an upcoming section. The scope of this thesis is to address the issues with the existing skull simulator and come up with an upgrade on the existing model. The skull simulator remains the only objective standard for impedance measurement in the industry. There is two commercially available skull simulators in the market now - SKS 10 from Interacoustics A/S Denmark and the Verifit skull simulator VA300 from Audioscan, as shown in Figure 2.17 [36].

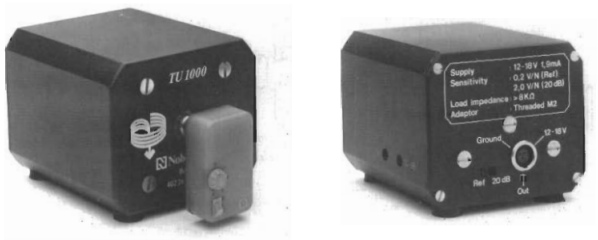

Figure 2.16: TU1000 Skull Simulator. [39]

Figure 2.17: TU1000 skull simulator with commercially available skull simulators SKS10 and Verifit, respectively. [36]

2.5.3 Head Simulator

Head simulator was developed internally at Cochlear by Henrik Fyrlund and his colleagues. There was a need for the head simulator because the skull simulator's mechanical impedance values (MPI) were conflicting with the CR values (as shown in figure 1.1), i.e., the Woelflin's mechanical impedance values [38], which is widely used in the hearing implants industry for MPI values of the human head. Head simulator was the outcome of a project whereby a head surrogate, which includes the skin, skull, and brain substitutes, could reliably mimic the MPI values and correlate with the CR values.

The current head simulator consists of a sphere filled with a brain surrogate material and an artificial skin on top. This assembled head simulator was able to produce comparable results to CR as compared to the skull simulator. However, it is still not an exact match with CR values and there exists scope for improvement of the current head simulator. Also, the brain surrogate, degraded with time, thereby resulting in variability in results. It was also susceptible to degradation owing to microbial attack. This thesis project is intended to overcome these issues and scale the same concept later on an anatomically correct artificial head to improve the impedance match with the CR values.

2.6 Parameters

2.6.1 Mechanical Point Impedance

Mechanical Point Impedance (Z) is the structure's, in our case the skull bone's at the stimulation site, resistance to vibration velocity (V) when subjected to a force excitation (F) from the sound processor of the hearing implant. The greater the value of impedance magnitude the lower would be the vibrations induced owing to stimulating force. Peak impedance is observed at the anti-resonance frequency, thereby the vibration velocity is drastically reduced. MPI (Z) could be defined as the complex quotient of magnitude and phase, between the force which is applied with its unit in Newton and the ensuing vibration velocity with its unit in meter per second [36][40].

$$Z = F/V[Ns/m] \tag{2.1}$$

2.6.2 Transcranial Attenuation

Transcranial attenuation (TA) can be defined as the difference in sensitivity or perception arising due to the differences between the ipsilaterally and contralaterally transmitted bone conduction sound when the stimulation is at a similar position on either side of the cranium. This stimulation position can either be the mastoid bone which is part of the temporal bone or the parietal bone where the BCDs are usually implanted [41]. A positive value indicates a much stronger response at the ipsilateral side in comparison to the contralateral side. The amount of masking needed for bone conduction hearing threshold could be estimated through the estimated TA values [42][43].

2.6.3 Acoustic Feedback

Acoustic feedback (AF) arises due to the coupling and relationship between the receiver and microphone in the external sound processor, which is attached close to the ear. This is typically a feedback loop from the sound processor output till sound processor input as it is illustrated in Figure 2.18. Typically this leads to a ringing or howling sound in the hearing implant. Owing to this, some of the earlier hearing aids had a microphone along with one ear and the receiver at the other ear, to overcome these undesirable AF effects. This is highly undesirable and leads to a reduction in the maximum attainable gain. It can be suppressed through various techniques, as it shall be discussed in the studies about AF section [44][45].

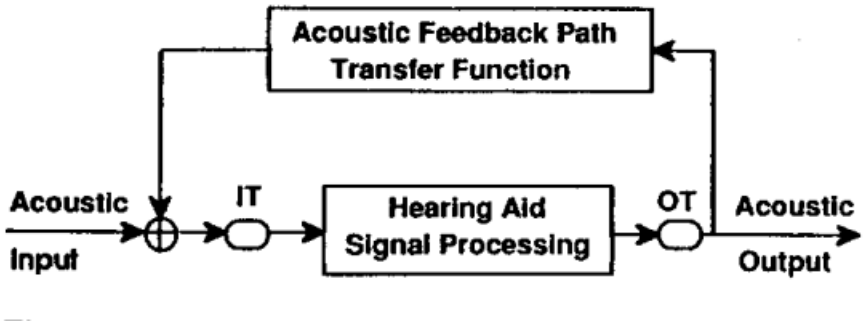

Figure 2.18: Schematic illustration of AF path. [46]

2.7 Existing Studies on Parameters

2.7.1 Mechanical Point Impedance

Woelflin [38], investigated the mean MPI values on 45 patients, with seven patients in Gothenburg, Sweden, and the remaining 38 in Edmonton, Canada. Proper calibration and mass compensation were performed for the measurement setup. Even though the measurement setup and procedure were different at both these sites, they were later proved to be equivalent. Also, the impedance measurement system was proved to be linear. The results were comparable to the previous study [40] with the anti-resonance peak appearing at 147 Hz. Patients with age older than 60 and those who had surgery have a lesser value of MPI as compared to younger and patients without surgery respectively. A smoothed version of MPI was modeled based on second-order system with one zero and two underdamped poles. Intersubject variation was also observed due to the implant's angle of implantation. Noise in the acceleration channel was found to affect low frequencies. Two snap couplings from Cochlear BAS and Oticon Medical were investigated and Oticon's coupling was found to be 15% softer and hence has a lower resonance peak. However, the cochlear's snap coupling is made of plastic and prone to long-term wear and tear, which implies a role reversal in the long term.

Hakansson et al.[36], measured MPI using data from the same 45 subjects (seven in Gothenburg, Sweden and 38 in Edmonton, Canada) in the study by Woelflin [38]., and

examined the variability of results according to age, gender, ear surgeries, and malformations. The conclusion from the study is that the first anti resonance peak is observed at 150 Hz. Below this frequency, the impedance response is mass controlled and above this frequency, it is spring controlled. At high frequencies, it is mass controlled as impedance response depends on the implant and surrounding bone. Impedance characteristics change for age over 60 and patients with major ear surgeries. No variability was found owing to gender, skull abnormalities, or even the type of snap coupling used. In related earlier work, Hakansson et al. [40], measured the MPI values for both the skull and the skin-covered skull. The conclusions from that study were that skin covering the skull had their impedance characterized by skin and its associated subcutaneous tissue. Therefore, the impedance magnitude of the skin covered skull was 30 dB less in comparison to MPI values measured directly on the skull owing to attenuation. Hence direct skull stimulation required lesser force to induce vibration. An eight parameter impedance analogy was also developed successfully.

2.7.2 Transcranial Attenuation

Stenfelt et al. [41], performed pure-tone hearing threshold test on 31 unilaterally deaf patients with a frequency range between 250 Hz and 8000 Hz. They were stimulated at four different positions - ipsilateral and contralateral mastoid, ipsilateral and contralateral Bone Conduction Hearing Aid (BCHA) position. The results showed that during stimulation at mastoid, the mean TA was 3 to 5 dB up to 500 Hz, close to 0 up to 1800 Hz. This attenuation subsequently increased to around 10 dB at the frequency range 3000-5000 Hz and then reduces slightly at the highest frequency with a value of 4 dB at 8000 Hz. When stimulated at BCHA position, the corresponding values were of the order 2-3 dB less. Another observation is large inter-subject variability for TA values of the order of 40 dB, but the general trends of TA remain the same with minimal difference. They concluded that median TA values depend on the stimulation position and frequency group.

Snapp et al. [47], measured TA values of 27 patients with unilateral SSD with 14 males and 13 females (average age of 55) at different frequencies from 500 Hz till 4000 Hz. The current FDA guideline is pure tone average (PTA) of 20 dB for a normal ear in the above-mentioned frequency range. Hence SSD patients with PTA less than 20 dB were deemed suitable for surgical implantation of any bone-anchored implants (BAI), like the BAHA or BCI, which is a bit flawed measure. The goal of this study was to estimate whether TA could provide predictive benefits assessment for SSD patients who are to be implanted with BAI. Regression analysis was conducted as a statistical measure. Speech in noise (SIN) was deemed as the standard for those patients who are to be implanted with BAI, based on previous studies [48][49][50]. TA values did not show any correlation with SIN values, even at high frequencies. Adjusted PTA, which is the PTA added with TA values at the respective frequency, did not show any correlation with SIN measures. The correlation was found to be 0.01% and deemed negligible. The conclusion from this study is that TA values do not provide any predictive benefits for SSD patients implanted with BAI.

Rigato et al.[51], used 4 different transducer attachments - flat base (A), extended flat base (B), bar with a screw at each end (C) and a percutaneous attachment (D) to assess its effect on vibration transmission and TA in direct drive BCD. A, B, C are all attachments

at mastoid bone closer to the cochlea, for active transcutaneous devices, while D is a percutaneous attachment at the parietal bone. Stimulation applied was a swept sine between 0.1 and 10 Khz. Vibrations along cochlear promontory were measure for A, B, C attachments along both ipsilateral and contralateral sides using laser doppler vibrometer and through ear canal sound pressure measurements with a microphone inserted into the middle and inner ear. Results showed that attachment C with two screws, showed was most effective for transmission around 6KHz but lower transmission at mid-frequency ranges. Also, lower contact was deemed to be an advantage for vibration transmission. Attachments A, B, C were compared and normalized according to attachment D, both along the ipsilateral and contralateral side. A, B, and C had TA ranging from -10 till 0 dB for frequencies below 500 Hz and varying between 10-20 dB for high frequencies. D had lower TA values at 500 Hz. Trends are comparable along both ipsilateral and contralateral sides.

Mackey et al. [52], investigated how the maturation and development of skulls with age, influenced the BC sensitivity through an indirect measure of BC attenuation. 76 individuals participated in the study including 59 infants and 17 adults. Transducers were placed at the ipsilateral and contralateral mastoids, forehead positions to provide the stimulation. The attenuations were measured through the introduction of a probe in both ear canals which measures these attenuations. Both transcranial and forehead attenuation were measured. Bone attenuation was calculated as the difference between forehead and TA. Generally, the forehead attenuation had a higher magnitude than TA, the attenuation was maximum at 1000 Hz, minimum at 500 Hz, and 4000 Hz. Results showed that infants and children experience more bone attenuation than adults with a matured skulls. This is because the infant skull has fontanelle and big sutures. Also, it was observed that mid-ear development in infants was limited, however, it did not cause variability in readings. These clinical results along with relevant previous studies were taken into consideration for fitting the infants/children with Bone Anchored Hearing Systems (Bahs). Bahs fitting procedures were deemed to be effective on infants with SSD or uni/bi-lateral hearing loss, owing to them having a compact bone, which facilitates routing of vibrations from ipsi to contralateral side, thereby improving SIN performance.

Li et al. [53], investigated various experimental and numerical methods for assessing the vibration modes and TA in single-sided BC hearing. One of the major factors which affects sound localization is the transcranial transmission, which is affected by the transfer function of various pathways and whole head vibration modes. The goal of this study is to estimate the frequency dependence of BC vibration modes, the contribution of the middle and inner ear to hearing perception, correlating the TA measurements from dynamic measurements and hearing threshold. Laser Doppler Vibrometry (LDV) measurements were performed on cadaver heads. Also, a whole head finite element (FE) model was proposed. Results showed that with an increase in frequency, the rigid motions transform themselves into local compression. Also, there are more fluctuations observed on the excitation side rather than on the contralateral side. FE studies showed that at low-middle frequencies, the inertial response of the ossicular chain was deemed critical for BC. Dynamic characteristics of the ossicular chain, with resonance at 1600 Hz, affect the frequency response of stapes and TM. The TA results had an upward trend in general except at frequencies around 700 Hz. Reason being that the excitation side had an opposite phase, while the contralateral side had a matching phase, with the net result being negative at these frequencies.

2.7.3 Acoustic Feedback

Dyrlund et al. [44], investigated a prototype Digital Feedback Suppression (DFS) system on hearing aids and its potential benefits in improving the AF margins. 21 behind the ear (BTE) patients and four In the ear (ITE) patients were involved in the study. Special Complex loop measurements were conducted in an anechoic chamber to assess the potential feedback margin improvements in the hearing aids. DFS system adds an equivalent input sign with the opposite sign to the external feedback signal. The net effect is the neutralization of the external feedback loop. Results showed that the BTE group exhibited gain improvements of the order ten to 13.1 dB, apart from introducing a 180 degrees phase shift. ITE group had gain improvement margins of 9.8 to 16.1 dB for the normal condition and 13.7 to 16.3 dB for 180 degrees phase shift condition. This 180 degrees phase shift in BTE aids does impact the feedback frequency and feedback margin improvements. This DFS may help in eliminating the amplitude distortions owing to it nullifying the output feedback loop. This will bring about increased sound quality in the hearing aid.

Bustamante et al. [46], tested three AF suppression techniques - time-varying delay, adaptive inverse filtering, and Adaptive Feedback Cancellation (AFC). The spectral content of the AF path depends on the transfer function of the hearing aid and the AF path. Also, in-situ measurements involving BTE hearing aids are affected by the changes in the acoustic environment emphasizing the need for adaptive methods of feedback suppression. Time-varying method introduces a delay in the signal path of the hearing aid thereby altering the phase values, thereby disrupting the feedback loop. This leads to a small gain of one or two dB and moderate distortion. This technique is deemed not optimal for use in a hearing aid. Adaptive inverse filtering involves the introduction of just a narrow-band notch filter or a delay along with the notch filter. This filter attenuates both the input signal and feedback loop, deeming it unsuitable. The fixed delay was kept at 0.8 milliseconds. When they used a twelve coefficient adaptive filter the resulting gain was three to four dB, which was a bit lower than desired. AFC method was deemed to be the best technique to suppress feedback of the three techniques considered. The feedback signal was estimated by filtering the hearing aid output with the AF path transfer function. This was modeled as a delay followed by the FIR filter. Delay was set at 0.85 milliseconds and the FIR filter used is short, which reduces the computation time. AFC with six and twelve coefficients produced a gain of six to eight dB and eight to ten dB respectively. There was no improvement in sound quality with AFC methods. This increase in gain of six to ten dB has the potential to benefit moderately impaired patients.

Sankowsky-Rothe et al. [45], probed a reciprocal measurement technique for measuring AF path. This reciprocal measurement was compared with direct measurements on a dummy head, at the same time varying the factors which could impact and affect the AF path such as venting, output sound field, inner ear geometries. Results showed minor differences between the two and overall agreements. Crucially the ear canal sound pressure was reduced by 30-40 dB for reciprocal measurements in comparison to direct measurements.

Sankowsky-Rothe et al. [54], worked on modeling the AF path for hearing aids. Adaptive

filters are needed to reduce AF. To make the adaptive algorithms less computationally expensive and to increase their computation speed, the AF path has been divided into time-invariant fixed path and time-varying variable past. This fixed part could be estimated through two approaches - a digital filter design that makes use of two microphones in the hearing aid, and a physical location approach which uses an electro-acoustic model along with microphones each in the hearing aid and ear canal. This individualization leads to increased performance and a reduction in the total number of variable coefficients from 40. Similar results were obtained from both approaches, especially when we consider the added stable gain values. Both approaches have certain trade-offs with the physical location-based model needing a microphone in the ear canal and reduced effort for hearing aid fitting. On the other hand, the digital filter design model requires more effort for hearing aid fitting but independence of hearing aid design.

2.8 Simulation Studies

Kim et al. [55], developed a three-dimensional finite element (FE) model with added polyurethane (PUR) of the human dry skull. This is useful in understanding BC and the dynamic characteristics of the head. For validating the model, the results with the FE model were compared with experimental results for MPI and acceleration at ipsilateral and contralateral cochleas. Results were in agreement for MPI values and the acceleration response along the lateral medial side. There was a discrepancy for the acceleration response along the inferior-superior side. Additionally, this FE model of the dry skull also helps in predicting the vibration response along with the middle and inner ear bones.

Chang et al. [56], developed a FE model of the whole human head, with eight components - brain, cerebrospinal fluid, outer cortical bone, a spongy layer called diploe, inner cortical bone, soft tissue, cartilage, and eye, as shown in the Figure 2.19 . This model was developed from cryosectional images of a female. The simulation results were compared with experimental results obtained from cadavers and live human subjects for parameters such as MPI, transcranial BC sound transmission, vibrations of cochlear promontories. Results showed multiple low-frequency resonances, with the first one caused due to rotation of the head, the second one being close to the resonance response of cadaver heads. At high frequencies, the simulation and experimental average results vary by the order of one standard deviation. The acceleration response at cochlear promontories was generally lower for simulation in comparison with the experimental results but the overall trend is the same. With this simulation model, the dynamic characteristics of the BC sound transmission could be predicted.

Chang et al. [57], again used this FE model of the head to evaluate the power distribution and power flux transmission, when stimulated by mechanical vibrations at the mastoid position. Results showed that the cortical skull bone, which occupies the least volume in the head is involved the most in BC power distribution and transmission. Soft tissues and cartilages are second, which occupies the largest volume in the head. The skull interior which is the brain and spinal cord contributes least to power transmission, especially with the neural tissues. Power transmission is mainly on the surface of the brain at the brain bone interface. This vibration transmission mainly concentrates at the skull base

and occipital bone. Power transmission is minor at the face, forehead or vortex. At high frequencies, there is more power loss compared to mid and low frequencies and power loss increases with distance from the excitation point.

In another related study, Chang et al. [58], compared various models of BCD - three direct drive, four skin drive, and one in the mouth device on the FE model. It is not easy to compare BCDs experimentally on the same conditions and subject, as most of them need to be implanted. The driving force were given as input and voltage was then applied to the motor of BCD's driving unit. Responses of all BCD's were similar to 500 Hz. At high frequencies above 4 kHz, direct drive devices such as BCI and Bonebridge provided a slightly better cochlear response than baha/ponto and Soundbite. Skin drive BCDs such as sophono and baha attract gave a similar cochlear vibration response to direct drive BCDs at low and mid frequencies up to 2 KHz, but the lower response at higher frequencies. Radioear B71 showed both extremes - highest response at low frequencies and lowest response at high frequencies. Adhear meanwhile gave a consistently low response irrespective of its frequency. Overall, this study has accomplished the almost manually impossible task of comparing BCDs under the same conditions which have the scope in facilitating convenient design and improvement of BCD's.

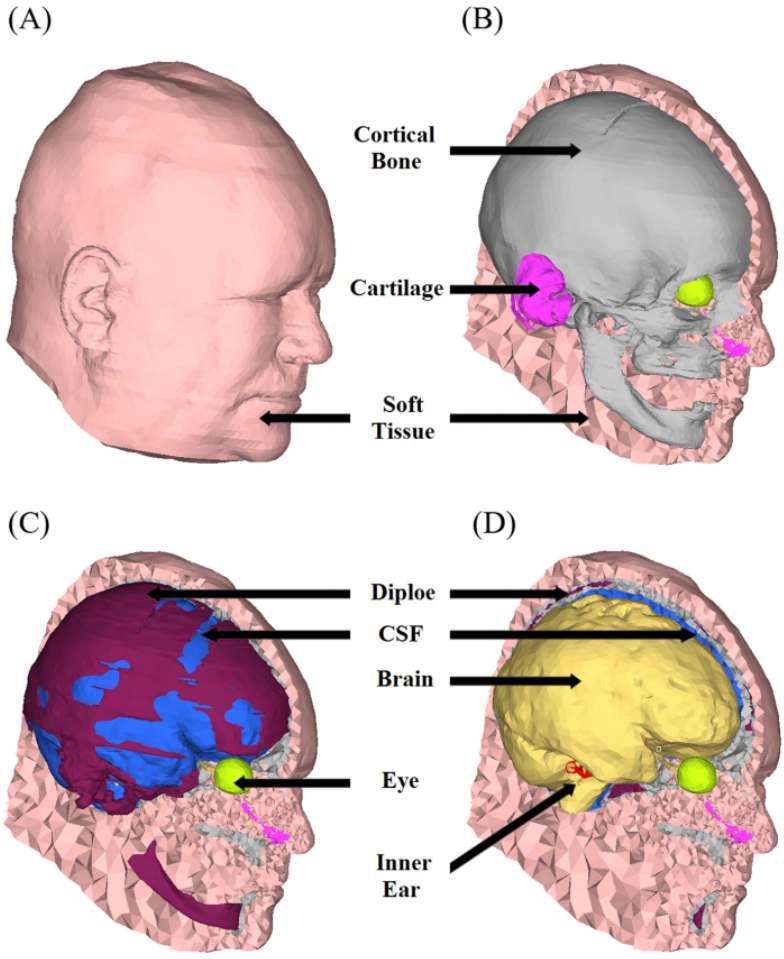

Figure 2.19: Various components of whole head Finite Element model - LiUhead (A-D). [56]

2.9 Existing Studies on Material Selection

2.9.1 Skull

Due to the various limitations and restrictions associated with the use of human cadavers and Post-Mortem Human Surrogates(PMHS), as discussed earlier, various researchers have investigated and come up with an artificial/synthetic skull bone surrogates, for usage and testing under laboratory conditions for a range of studies and applications. Some of the prominent ones shall be discussed in this section.

Brown et al [59], investigated the commercially available skull stimulants such as Synbone (6mm 3 layer PUR), Sawbones (7mm 3 layer composite) and Bonesims (7mm 3 layer made of bovine bones) for its mechanical response when subjected to quasi-static and dynamic loading. All the simulants exhibited strain rate dependant characteristics. Based on correlation of the results with their corresponding values measured from human skulls, Bonesims was chosen as the best surrogate due to favorable results obtained for parameters such as Young's modulus (1500 MPa), Ultimate strength (49 MPa), Yield strength (19 MPa) and Ultimate strain (17%). Plaisted and Gardner et al. [60], worked on developing cranial surrogates mimicking the layered and porous architecture of human cranial bones using the Stereolithographic (SLA) Additive Manufacturing(AM) method. XC 11122 is the chosen surrogate material which is Acetonitrile Butadiene Styrene(ABS) like photo-polymer. The porous diploe region was accomplished using a repeating unit, with controlled pore diameter and thickness to meet the set target values. A transparent and low modulus material was also used to facilitate fabrication and post-processing. This prototype was able to achieve comparable beam stiffness and failure characteristics to human cranial bones.

Falland-Cheung et al. [61], investigated five skull simulant materials for parameters such as elastic modulus and flexural/tensile strength. The five stimulant materials tested were Epoxy Resin (ER), Fibre-filled Epoxy Resin (FFER), Poly Lactic Acid (PLA), Polyethylene Terephthalate Glycol Modified (PETG), self-cure acrylic densure base resin. It was found that ER and FFER exhibited values closer to the mean human values of elastic modulus and tensile strength. However, FFER exhibited high values for flexural strength compared to other simulants, owing to the presence of fibers. PLA gave the closest match to fracture properties at high strain rates. They concluded through this study that ER was suitable surrogate material for low impact applications while PLA is ideal for high impact blunt force tests and applications. Roberts et al.[62], worked on developing a human cranial surrogate for impact testing and studies. They used ER with milled glass fibers for both the internal and external tables (two mm each) and urethane foam (four mm) for the diploe region of the synthetic cranial bone. They were able to achieve comparable results for bending strength, tensile strength, and fracture toughness of human cranial bone. Drop tests were also performed. The force required to fracture a sheet of the developed material was low compared to human cranial bone, however, the fracture pattern was found to be comparable.

2.9.2 Brain

Numerous brain surrogates have been employed in various studies by researchers, which shall be covered in this section.

Forte et al. [63], developed a novel Composite Hydrogel (CH), which was synthesized with 6% concentration of Poly Vinyl Alcohol (PVA) and 0.85% of Phytagel. The CH was compared with other commercially available surrogate materials such as Sylgard 527/184, Hyaluronic Acid, Gelatin for mechanical properties when subjected to compression and loading. It was found that CH exhibited values close to corresponding the brain values found in the literature for properties such as compression, indentation, relaxation, hysteresis, and shear. The CH is also suitable for complex deformation scenarios such as brain shift. They also used this CH, as part of a life-sized phantom with a 3D printed Acrylonitrile Butadiene Styrene (ABS) skull, which could be used for investigating the TBI studies. To mimic the surgical cutting properties, they varied the concentration of PVA in CH from 6% to 2.25% and Phytagel from 0.85% to 1.1% to get the desired results. Tan et al.[64], used the same CH to produce a life-sized brain phantom for demonstration and also a varied concentration of PVA and Phytagel for surgical training on the brain for tumor removal. It also includes a detailed explanation of the manufacturing procedure of CH, which is quite simple, easy to prepare, non-toxic and its constituent compounds are widely available.

Liebinger et al. [65], investigated two commercially available materials such as Gelatin and CH for needle insertion and fracture behavior tests. Initially, the stiffness was matched for both Gelatin and CH, which formed Modified Composite Hydrogel (MCH), by comparing it with the porcine brain, which is widely accepted in the literature as being comparable in properties to the human brain. The needle insertion tests showed that Gelatin had comparable values with a porcine brain, whereas MCH exhibited comparable viscoelastic properties. Hence while selecting a surrogate material both material properties and tool tissue interactions, must be taken into consideration. Both Gelatin and MCH showed agreement with few brain properties, but neither of them could be considered a perfect surrogate as each has their limitations. Chanda et al. [66], developed a two-part silicone-based brain, which could mimic the biofidelic properties of the human brain. This two-part representing the grey and white matter of the brain was sourced from Smooth-On inc., and has a Shure hardness of ten. Five Hyperelastic curve fitting models were used to characterize its non-linear mechanical response. The three-parameters Yeoh's model was adjudged to be the most accurate owing to the average correlation index of 0.997.

Finally, Singh et al. [67], compared the standard which is the porcine brain with some brain simulant materials such as bovine gelatin, agar gelatin, and sylgard 527. Ogden's hyper-elastic fitting method was used for comparison with the porcine brain values. It was found that bovine gelatin with both 3% and 5% concentration had comparable values for quasi-static loading. Alternatively, both agar gelatin and Sylgard 527 were comparable for sinusoidal compression. Hence there is variability in results with different strain rates and loading. The study concluded that no of the tissue simulants were ideal and do have their drawbacks.

2.9.3 Skin

There have been various skin models developed which can be grouped into two categories: bio-based skins and artificial or synthetic skins. For this project, only synthetic skin is of interest and deemed suitable. Dabrowska et al. [68], developed a gelatin-based skin on a cotton cloth substrate which gets cross-linked in a Glutaraldehyde/PBS (Phosphate Buffered Saline) bath. This skin is rubbed against Martindale fabric, which is a standard textile under both moist and dry conditions. This is done to characterize its frictional behavior, in particular average friction coefficient. They also estimated Young's modulus, thickness, and surface morphology under both moist and dry conditions. The results obtained were largely comparable to the corresponding values of human skin, which was tested in-vivo.

Chanda et al. [69], developed a novel elastomer-based synthetic skin to mimic the non-linear mechanical properties of human skin. This skin consists of two-part silicone with Shure hardness of 00-10 in contact with a stiffer silicone with a shure hardness 30A. Hyperelastic characterization was performed, elastic modulus at a low and high stretch, ultimate tensile stress were measured and compared with natural skin values and were found to agree with their respective values. This biomechanical mimicking of biofidelic skin had one major limitation, with it being an isotropic material in comparison to the natural skin, which is anisotropic. Dabrowska et al.[70], discussed the various materials which could be used to mimic the physical properties of human skin such as liquid emulsions, gelatin, polyvinyl-acrylate (PVA), PUR, ER, and metals. This was a purely theoretical study and debated the suitability of each material for a particular application and physical property.

Whittle et al. [71], developed a two part skin layer - PUR foam representing a sub-dermal layer and a silicone layer representing the epidermis. This was subjected to blunt force trauma impact to investigate the dynamics of blunt force wounding. Internal/external wounding, lacerations generated were analyzed. The only 48.6% of impact resulted in external wounds while 96% of an impact led to internal wounds, which in a way explains the hematoma formation and contusions.

3
Materials and Methods

3.1 Materials Selection

3.1.1 Skull Surrogate

Various materials have been used as skull substitute material in scientific studies. Chief among them are PUR foams, various combinations of ER and ABS when the skulls are 3D printed. Some commercially available materials which were interesting and relevant for this project include PUR materials from both Sawbones and Synbones, composite material from Sawbones, bonesim material which mimics both the cortical and cancellous regions of human bone, undisclosed material from Phacon, which mimics the three-layer structure of human skulls: outer table-diploe-inner table.

3.1.2 Brain Surrogate

Gelatin made from agar and beef powders, which were mixed with either glycerine and water or glycerine and sorbitol were considered initially. The problem with these solutions is that they experienced degradation and microbial contamination with time, as a result of which, they are unstable and introduced variability in results over time. Lots of ballistic studies have used 10% ordnance gelatin. Some examples for these ballistic studies include defense studies by the army, for assessing the impact on head due to blasts, TBI studies, assessment of bullet penetration through the head, and so on. Unfortunately, ordnance gelatin also suffers from stability and durability issues, which makes it unsuitable for our application.

Previously, silicon rubber was used as a brain phantom during an experimental study at Cochlear and was found to be unsuitable for our application. This is because it was stiff and produced high damping resulting in an uncharacteristic impedance plot in comparison with the CR values. Dielectric silicone gels such as Sylgard 527 and Sylgard 184, also called Polydimethyl Siloxane (PDMS), were used in various scientific research studies as a crude brain substitute with mixed success. Sylgard 184 has a shure strength of 43, which is reasonably hard and stiff. Due to this concern, doubts existed if it could mimic the soft and sensitive human brain. Sylgard 527 A and B, was used more commonly than Sylgard 184 as brain phantom. But since it was expensive and also had 9 weeks of waiting time for delivery, its experimentation was postponed to a later date, even though it is a material of interest to this author and my supervisor at Cochlear.

The next material under serious contemplation as a brain phantom material was the CH material which could mimic the human brain mechanical properties. It was developed

by Dr. Antonio Elias Forte and his team namely, Dr. Zhengchu Tan. It was the most promising material in terms of reliably mimicking mechanical properties like compressive stress, stiffness, hyper-elastic behavior, rate-dependent characteristics, etc [63]. This is a composite material made up of Polyvinyl Alcohol (PVA) and phytagel, a tetrasaccharide, along with distilled water [64][63]. In one of the articles, the author mentions that the CH material which is synthesized, will remain fresh up to 3 days [63], but long-term stability is an unknown quantity. Other studies showed that CH easily degrades with time and hence it is not a long-term solution for our application. Hence this option was deemed to be a non-starter as well.

The final choices were synthetic gelatin, permagel, and soft PUR foams. For our application, it is paramount that the material must be non-aqueous, synthetic apart from being able to mimic the mechanical properties of human brains. The inorganic and synthetic gelatin number 5 was procured from Humimic Inc., USA. This material does not have water and uses mineral oil instead. Also, certain additives are added to synthetic gelatin, to make it soft and could mimic brain tissues. This material fits our requirement on paper and it is to be used as a brain phantom material for the first time. A substitute to gelatin called permagel was procured, which is again non-aqueous, synthetic, and can produce results similar to ballistic gelatin. This was procured from the brand Evi-Paq through its Sweden distributor "CLP systems". Both synthetic gelatin and permagel were procured as blocks and melted in the ovens before casting. The final choice for the brain phantom material is the PUR foams, which were used in a literature study before. Specifically, a soft variant of PUR foam material was chosen, which could then be cast to form a solid, flexible, and open-celled material, to match the brain material properties. Three variants - FlexFoam-iT! 14, FlexFoam-iT! 6 and FlexFoam-iT! III have been shortlisted based on the above criteria as well as its texture and feel. FlexFoam-iT! III has 18x expansion capabilities, while the other two expand 10x. These choices of PUR foams are completely experimental given the novel nature of our requirement.

3.1.3 Skin Surrogate

Extensive research studies showed silicone and latex are commonly used skin substitutes. At Research Group for Surgical Stimulator Linz, they also use silicone oil to mimic the fat tissues in the skin.

3.2 Manufacturing Methodology

3.2.1 Artificial Skull

An artificial skull mimicking a human skull is quite difficult to accomplish. This is because the human skull bone is a combination of various bones like parietal, temporal, occipital, frontal, and mastoid bones. Each bone has its varying thickness, stiffness, and dimensions. This leads to varying attenuation profiles in each of these bones, leading to variability in MPI values in various positions of the skull.

As discussed in section 3.1.1 before, PUR and ER are the common material choices for the artificial skull. Manufacturing methodology includes molding, casting, 3D printing, AM among others. Molding seems to be a common choice, 3D printing is beginning to grow mainstream and AM is generally not preferred for developing a synthetic biofidelic skull. It was decided to go ahead with commercially available options, as manufacturers were unwilling to manufacture a lower quantity of heads. Skulls from Sawbones, Synbones, and Phacon were considered for this project.

Also, since five brain phantom materials were shortlisted, which were untested for the parameters which are to be measured, an order of five PUR spheres from Synbone was placed. These spheres were found to mimic the mechanical properties of the human head, in a previous in-house experiment/study conducted at CBAS by Henrik Fyrlund and his colleagues. Hence the idea was to test the brain phantom materials on spheres first, before proceeding onto anatomically correct half skulls at a later date.

3.2.2 Artificial Brain

Various options were considered for the brain surrogate material and the rationale behind the final choices - PUR foam (Figure 3.2), synthetic gelatin (Figure 3.1) and permagel (Figure 3.3) were discussed previously in section 3.1.2. The material was melted in an oven, the molted material was directly cast into the head and then keeping the setup undisturbed so that it cools and solidifies. Post this step, the sphere with brain phantom material is ready to be tested with the measurement set up.

Figure 3.1: Synthetic gelatin from Humimic Inc. [72]

Figure 3.2: PUR foams from Smooth On Inc. [73]

Figure 3.3: Permagel from Forensics Source. [74]

3.3 Testing Methodology

3.3.1 Mechanical Point Impedance Measurement

This was the only measurement that was possible during this thesis project. The MPI values for six subjects, namely six spheres filled with brain surrogate substances such as synthetic gelatin, permagel, three types of PUR foams acquired from FlexFoam-iT series of Smooth-On inc. and an empty/hollow sphere were measured. All these spheres were implanted with BI-300 implants, as per industry norms and procedures as done in surgical implantation. At first, guides were used to fix the two positions which were opposite each other. A drill was used to make a hole at these positions, for the exact size of the BI-300 implant head, which ensures proper fit when BI-300 is implanted at the chosen points.

When it comes to the connection and measurement setup, it is important to calibrate the impedance head first. The impedance head 5860B (Figure 3.5), acquired from Dytran, has two output probes with piezoelectric crystals, which are used to measure the force and acceleration output of the spheres. The impedance head is calibrated by using a laser light from the laser doppler vibrometer with two known weights of ten grams and 50 grams, along with wax and stud as shown in the Figure 3.4. Any abnormalities during calibration was analyzed by connecting the output to a loudspeaker. A balanced electromagnetic actuator was connected with an impedance head and this setup was attached to the spheres using an adaptor, as shown in the Figure 3.6. Hence the final MPI value needs to be mass and phase compensated. The mass of the BI300 implant along with the adapter was estimated to be 4.125 grams. The internal mass of the impedance head was estimated to be 5 grams. Both masses need to be compensated. A PC-based signal processing system has been used. The mass and phase compensations were written into the Matlab script for getting measurement and magnitude/phase plots. Also, the stiffness below the accelerometer was estimated to be 4e8 N/M.

The impedance head connection is quite rigid. Another factor in the measurement setup (Figure 3.6) was the decoupling issue. Initially, soft foam was used for decoupling which was deemed to be not ideal for our measurement. However, the final readings were accomplished with the usage of a soft pillow, which made the measurements more consistent with similar measurements done on cadaver heads earlier. However, it is still not perfect and the readings taken below 100 Hz tend to be unreliable. The stimulation for the setup was provided from the actuator as white noise with 10 kHz bandwidth and the resulting output was measured through the force and acceleration gauge of the impedance head. A matlab script was written to interface the measurements and output the plotted results for both the magnitude of mechanical impedance (dB) and phase (deg). The vibration velocity needed for calculating the MPI values was obtained by integrating the acceleration values generated in the frequency domain. The scientific basis of calibration, mass compensation, and impedance measurement is discussed in the sections below for further understanding.

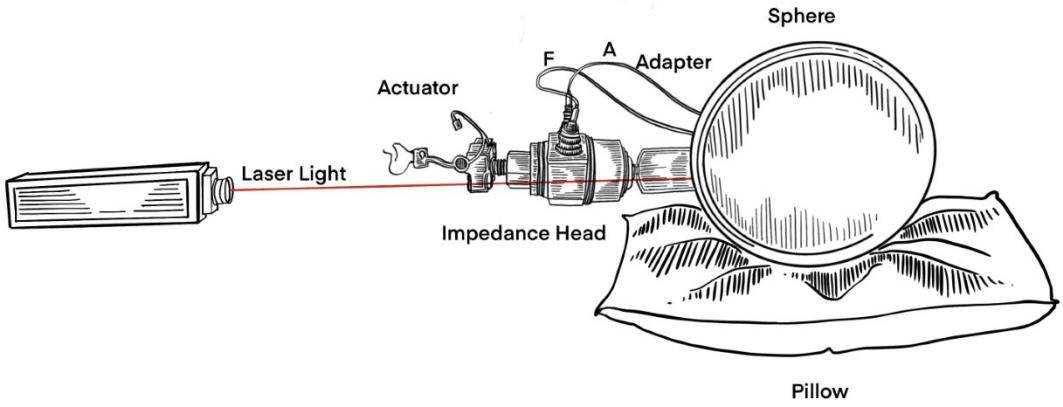

Figure 3.4: Calibration setup using a laser doppler vibrometer and known weights

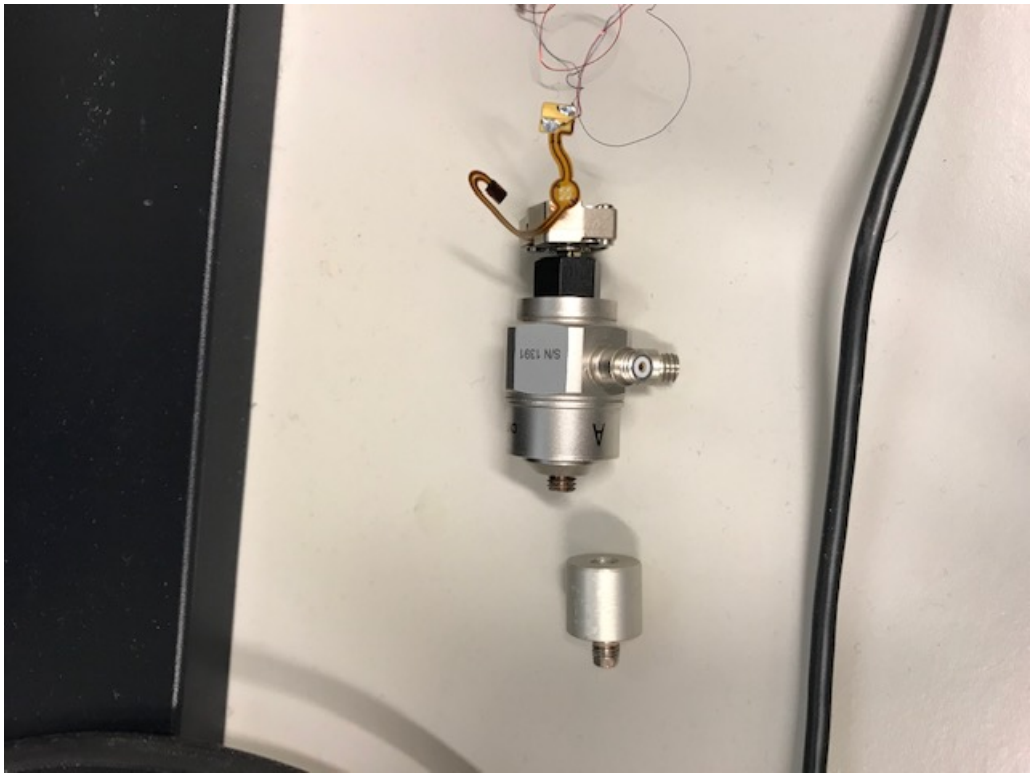

Figure 3.5: An impedance head with force and acceleration sensors.

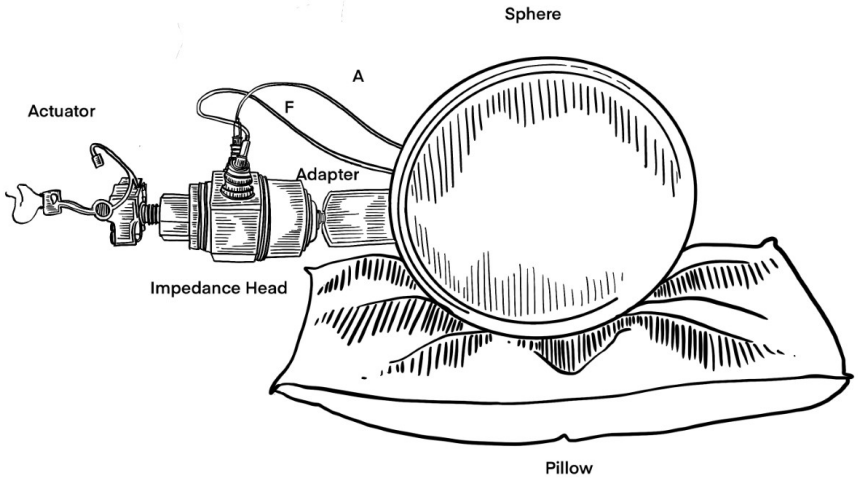

Figure 3.6: MPI measurement setup with balanced electromagnetic transducer or actuator, impedance head with force and acceleration outputs, connector, sphere to be tested supported on a pillow for decoupling

3.3.1.1 Calibration

Let the known weight of force gauge be "m1" and that of the adapter used for coupling with the implant be "m2". In order to find out the value of calibration constant K_c, we need to use a known third weight "m3", which could be mechanically coupled to the impedance head. The total mass then becomes $M_{tot} = m1 + m2 + m3$. The calibration constant could be found from the following equations:

$$M_{tot} = F/A * K_c \tag{3.1}$$

$$K_c = M_{tot}/(F/A) \tag{3.2}$$

$$K_c = (m1 + m2 + m3)/Q \tag{3.3}$$

Equation 3.2 must result in a constant value, particularly the total mass. However, this leads to an erroneous ripple formation in the impedance plots, which has a vector of values (F/A) instead of a constant. We cannot have these vectors for each frequency and to save time, a constant Q= (F/A) is calculated at 1000 Hz and used throughout the measurement. This leads to an estimation of the calibration constant as shown in equation 3.3 [38].

3.3.1.2 Mass Compensation

Masses of the adapter/snap coupling and also the impedance head's mass along the force gauge needs to be removed and compensated adequately from the impedance measurements. This is because impedance measurements include everything in the setup where there is any mechanical connection established [38]. Since we already know the calibration constant K_c, we can estimate the adjusted measurement quotient as follows:

$$Q_{adjusted} = Q_{measured} * K_c - (m1 + m2) \tag{3.4}$$

3.3.1.3 Impedance Measurement

Even though we estimated impedance values in a computer with a 64-bit floating point precision on the frequency domain, we have shown here an analog equivalent of the same, which is typically less accurate, for easier understanding. Since we already know the value of quotient Q=(F/A), this needs to be integrated to get the MPI (Z) [38]. This is accomplished through multiplication with an imaginary constant 'j' and frequency 'ω'.

$$Z = Q * (1/j * \omega) \tag{3.5}$$

$$Z = (F/A * j * \omega) \tag{3.6}$$

This results in the desired impedance

$$Z = (F/V) \tag{3.7}$$

4

Results

4.1 Sphere 1 - Synthetic Gelatin

4.1.1 Impedance Magnitude

The impedance magnitude plots for sphere 1 which is filled with synthetic gelatin, are shown in Figure 4.1. In all the spheres, measurements were taken with BI300 implant at either east or west positions on the sphere which are presented as E or W in the magnitude or phase plots. Similarly, the pillow's orientation used for decoupling is also varied from either a horizontal or vertical position which is presented as Horz or Vert in plots. This is done to check for the repeatability of results. Here the CR is presented as a curve in green color, sphere1EHorz is shown in light blue color, sphere1EVert is represented in orange color, sphere1WHorz is represented in grey color, sphere1WVert is represented in yellow color. The frequency values in the x-axis are represented in the logarithmic scale with its unit in hertz and the impedance magnitude has its units in decibels.

The impedance magnitude initially rises from 100 Hz with a positive slope in impedance magnitude and we can say that at these low frequencies, the response is purely mass controlled. Around 128 Hz, the first anti-resonance peak is encountered with a maximum impedance magnitude of 90 dB. At this point, there is an impedance magnitude difference of around 18 dB with the corresponding CR values. After this peak, there is a decrease in impedance magnitude and hence we can say this region is under stiffness control and represented through compliance instead of impedance. The impedance response however matches that of CR till around 576 Hz. At middle frequencies from 580 Hz till 1400 Hz, ripples are introduced in the measurements. This means that there is a continuous increase and decrease in the impedance magnitude at the region, thereby alternating between the mass and stiffness-controlled regions. This ripple behavior is undesirable and not in keeping with our clinical reference values.

The response is stiffness controlled until around 5000 Hz, which implies the decrease in mechanical impedance magnitude represented as a negative slope. At high frequencies beyond 3000 Hz, the impedance response shows a slight increase in impedance magnitude with a positive slope, thereby indicating a shift from stiffness-controlled regions to mass-controlled regions. At high frequencies, the impedance response is close to the CR, but still, some deviation in the magnitudes exists. At 8000 Hz, the magnitude deviation with CR is of the order of 5 dB.

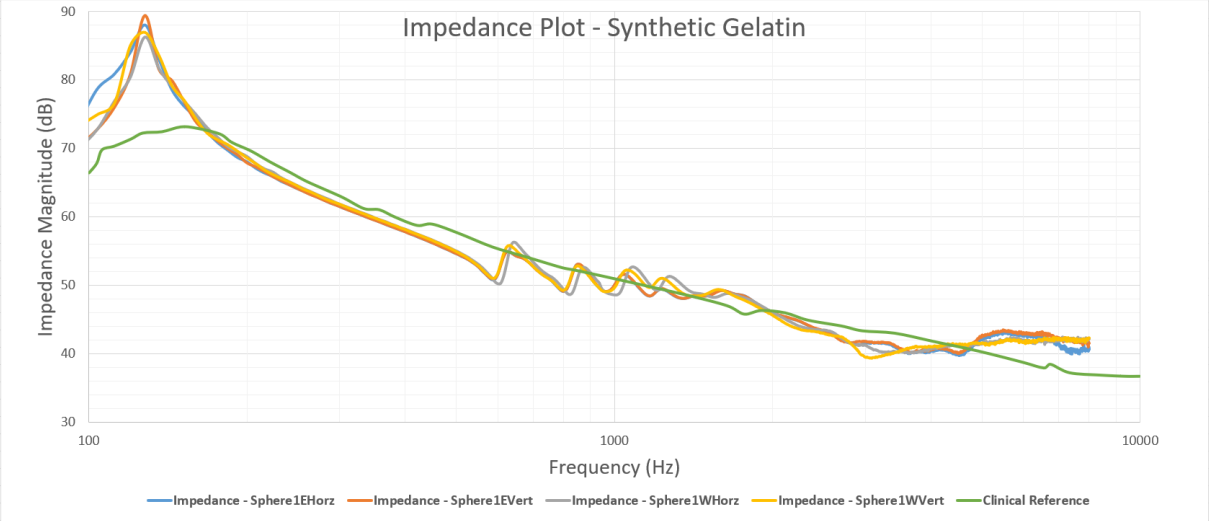

Figure 4.1: Impedance plot for Sphere 1 - inorganic gelatin.

4.1.2 Phase Measurement

The phase plots for sphere 1 which is filled with synthetic gelatin, are shown in Figure 4.2. The same color markings are used here as shown in Figure 4.1. The frequency values in the x-axis are represented in the logarithmic scale with its unit in hertz and the phase has its units in degrees.

At low frequencies around 120 Hz, there is a negative phase and significant difference with CR values. At mid frequencies, starting from 560 Hz till 1800 Hz, ripples are introduced in the plots, mirroring the corresponding impedance magnitude response curve. At high frequencies over 2000 Hz, the curve increases with positive phase, but again drastically different from the CR curve. At 8000 Hz, the difference between the plot and CR is around 102 degrees. The phase plot for sphere 1 does not match the CR values.

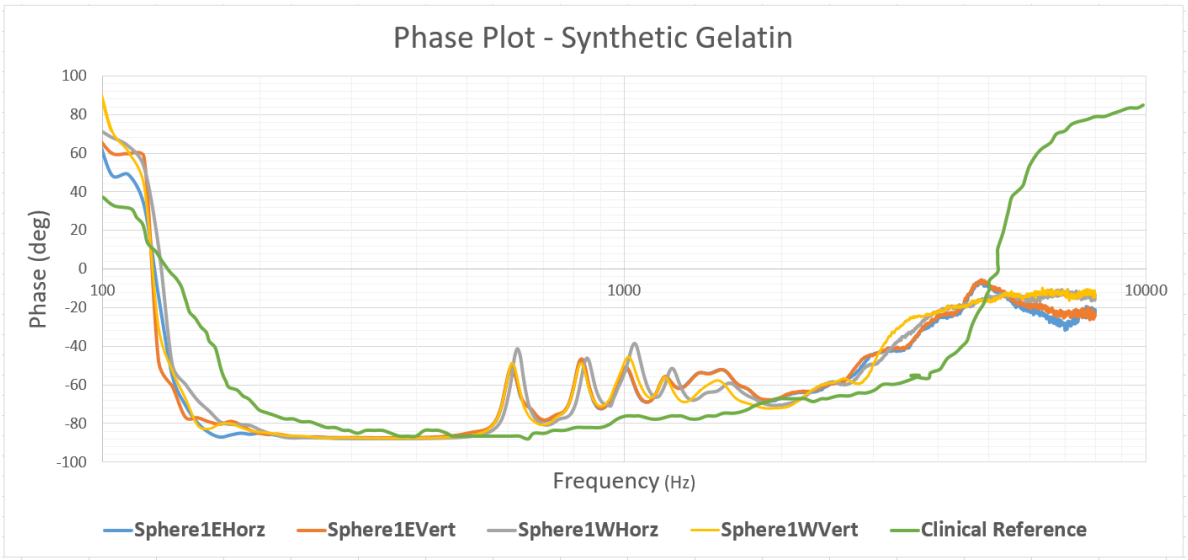

Figure 4.2: Phase plot for sphere 1 - synthetic gelatin.

4.2 Sphere 2 - Smooth On FlexFoam - iT™ 14

4.2.1 Impedance Magnitude

The impedance magnitude plots for sphere 2 which is filled with Smooth-On FlexFoam - iT™14, a variety of PUR, are shown in Figure 4.3. Here the CR is represented as a curve in green color. Sphere2EHorz is shown in light blue color, sphere2EVert is represented in orange color, sphere2WHorz is represented in grey color and finally, the sphere2WVert is represented in yellow color. The frequency values in x-axis are represented in the logarithmic scale with its unit in hertz and the impedance magnitude has its units in decibels.

The impedance magnitude initially rises from 100 Hz and it could be said that, at these low frequencies, the response is purely mass controlled as shown by the positive slope. Around 152 Hz, the first anti-resonance peak is encountered with a maximum impedance magnitude of 71.5 dB. After this sharp peak, there is a decrease in impedance magnitude, represented as a negative slope and hence this region is under stiffness control. A second anti-resonance peak is encountered at 304 Hz with a magnitude of around 67 dB. There is an increase in magnitude from around 224 Hz to the second anti resonance peak. At these frequency regions, impedance response is mass controlled which again changes to stiffness-controlled after the peak with a decrease in impedance magnitude. This second anti resonance peak is highly undesirable and not compliant with the CR values.

Post 1000 Hz, there is a significant deviation in impedance response in comparison with CR values and this region is still stiffness controlled with decreasing magnitude. Ripples start appearing at around 2296 Hz. This means that there is a continuous increase and decrease in the impedance magnitude at the region, thereby alternating between the mass and stiffness-controlled regions. This ripple behavior is undesirable and not in keeping with our CR values. The reasoning for these ripples is not yet known clearly and needs to be further investigated. This might be due to the inherent nature of the material, damping, or even some issues with measurement such as rigid coupling, decoupling issues, or insufficient mass/phase compensation. This ripple behavior continues in the high-frequency region until 8000 Hz, again highly undesirable for our need.

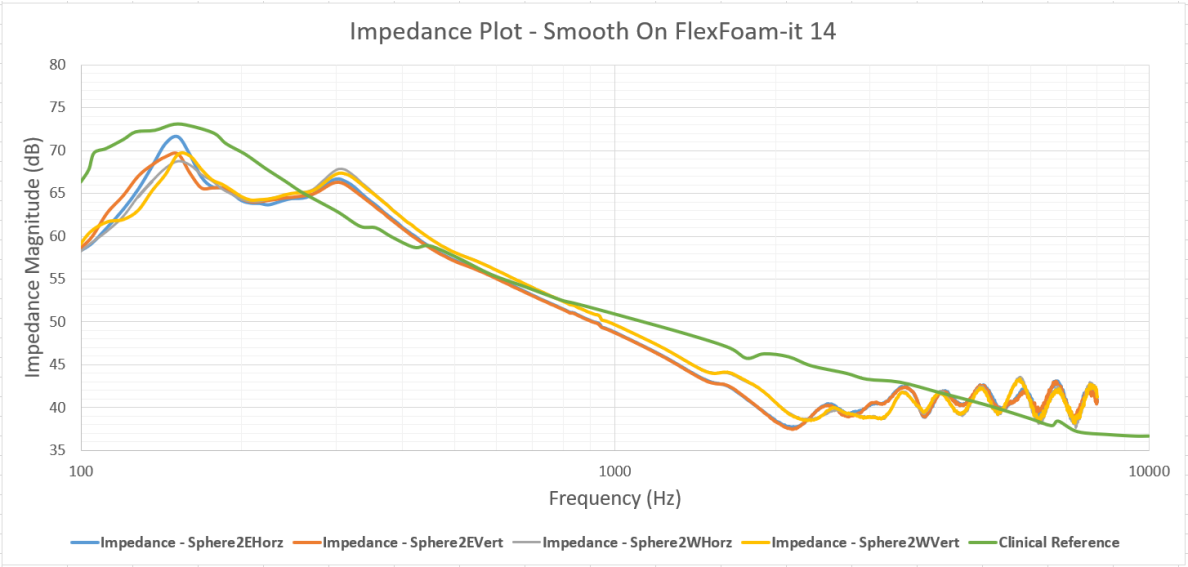

Figure 4.3: Impedance plot for sphere 2 - Smooth On FlexFoam - iT™ 14.

4.2.2 Phase Measurement

The phase plots for sphere 2 which is filled with Smooth-On FlexFoam - iT™14, a variety of PUR, is shown in Figure 4.4. The same color markings are used here as shown in Figure 4.3. The frequency values in x-axis are represented in the logarithmic scale with its unit in hertz and the phase has its units in degrees.

At low frequencies, there is a positive phase above 60 degrees. Around 160 Hz, a negative phase is encountered and the value decreases further. There are twin peaks in the low-frequency regions as the curve decreases in phase value and enters the negative phase. At mid frequencies over 400 Hz, the curve starts to flatten. At high frequencies around 2440 Hz, the curve increases in phase, and ripples are introduced. At 8000 Hz, the phase difference between the plots and the CR curve is around 97 degrees. The phase plot for sphere 2 does not match the CR values, as there is a vast difference between the plot and CR.

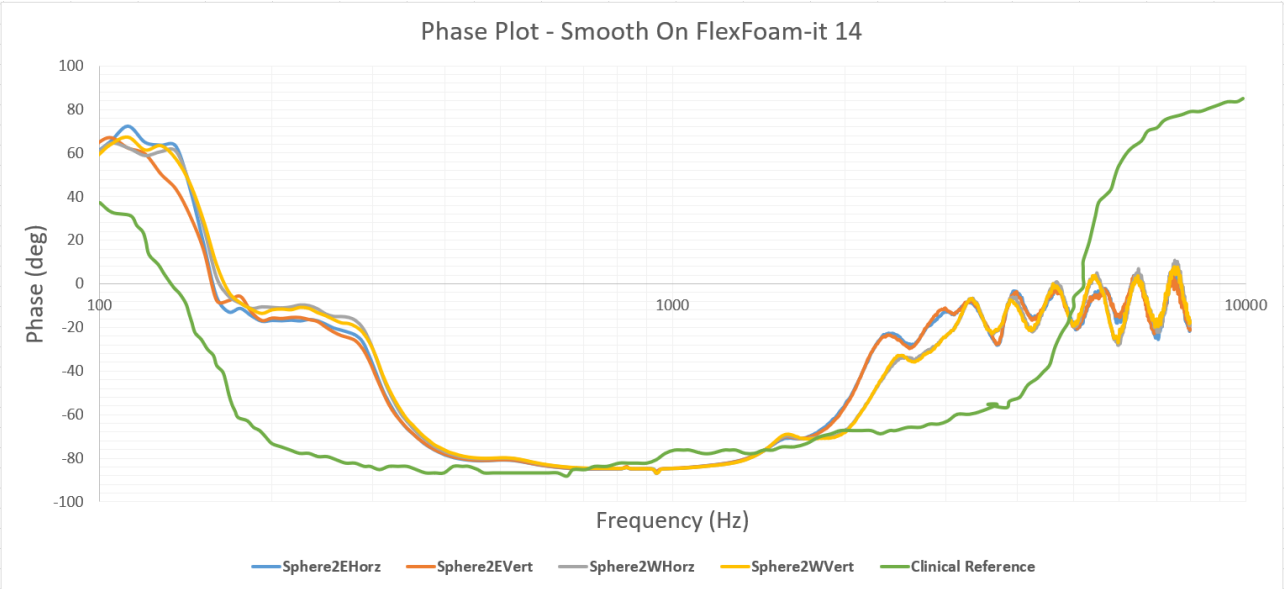

Figure 4.4: Phase plot for sphere 2 - Smooth On FlexFoam - iT™ 14.

4.3 Sphere 3 - Smooth On FlexFoam - iT™ 6

4.3.1 Impedance Magnitude

The impedance magnitude plots for the sphere 3 which is filled with Smooth-On FlexFoam - iT™ 6, a variety of PUR, are shown in Figure 4.5. Here the CR are represented as a curve in green color. Sphere3EHorz is shown in light blue color, sphere3EVert is represented in orange color, sphere3WHorz is represented in grey color and finally, the sphere3WVert is represented in yellow color. The frequency values in x-axis are represented in the logarithmic scale with its unit in hertz and the impedance magnitude has its units in decibels.

The impedance magnitude initially rises from 100 Hz and at these low frequencies, the response is purely mass controlled. Around 168 Hz, the first anti resonance peak is encountered with a maximum impedance magnitude of 74 dB. After this sharp peak, there is a decrease in impedance magnitude and hence this region is under stiffness control. A second anti-resonance peak is encountered at 232 Hz with a magnitude of around 69.66 dB. There is an increase in magnitude from around 208 Hz till the second anti resonance peak. At these frequency regions, impedance response is mass controlled which again changes to stiffness controlled after the peak with a decrease in impedance magnitude. A third anti-resonance peak is encountered at 328 Hz with a magnitude of around 67.55 dB. There is an increase in magnitude from around 288 Hz till the third anti resonance peak. At these frequency regions, impedance response is mass controlled which again changes to stiffness controlled after the peak with a decrease in impedance magnitude. These second and third anti resonance peaks are highly undesirable and not compliant with the CR values.

The impedance response matches the CR from 500 Hz until 800 Hz. Post 800 Hz, there is a significant deviation in impedance response in comparison with CR values and this region is still stiffness controlled with decreasing magnitude and represented as compliance

instead of impedance. Ripples start appearing at around 2240 Hz. This means that there is a continuous increase and decrease in the impedance magnitude at the region, thereby alternating between the mass and stiffness controlled regions. This ripple behaviour is undesirable and not in keeping with our CR values. The reasoning for these ripples is not yet known clearly and needs to be further investigated. This might be due to the inherent nature of the material, damping, even some issues with measurement such as rigid coupling, decoupling issues, or insufficient mass/phase compensation. This ripple behavior continues in the high-frequency region until 8000 Hz, again highly undesirable for our need.

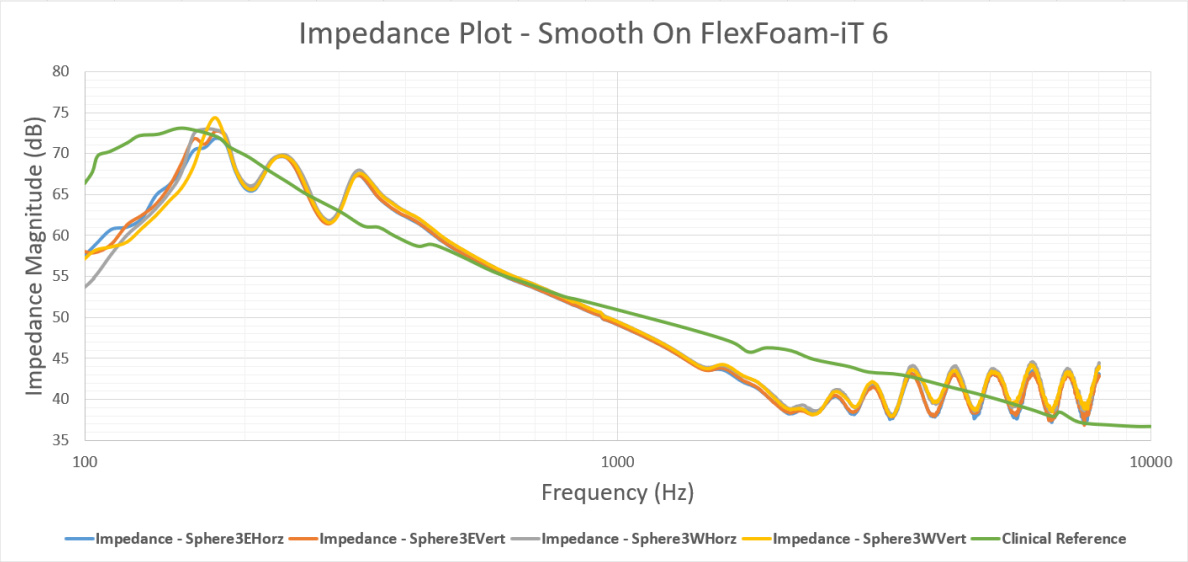

Figure 4.5: Impedance plot for sphere 3 - Smooth On FlexFoam - iT™ 6.

4.3.2 Phase Measurement

The phase plots for the sphere 3 which is filled with Smooth On FlexFoam - iT™ 6, a variety of PUR, are shown in Figure 4.6. The same color markings are used here as shown in Figure 4.5. The frequency values in x-axis are represented in the logarithmic scale with its unit in hertz and the phase has its units in degrees.

At low frequencies, there is a positive phase above 50 degrees and even closer to 100 degrees. Around 184 Hz, a negative phase is encountered and the value decreases further. There are three peaks in the low-frequency regions as the curve decreases in phase value, and enters the negative phase. At mid frequencies over 450 Hz, the curve starts to flatten. At high frequencies around 2550 Hz, the curve increases in phase, and ripples are introduced. At 8000 Hz, the phase difference between the plots and the CR curve is around 90 degrees. Phase plot for sphere 3 does not match the CR values, as there is a vast difference between the plot and CR values.

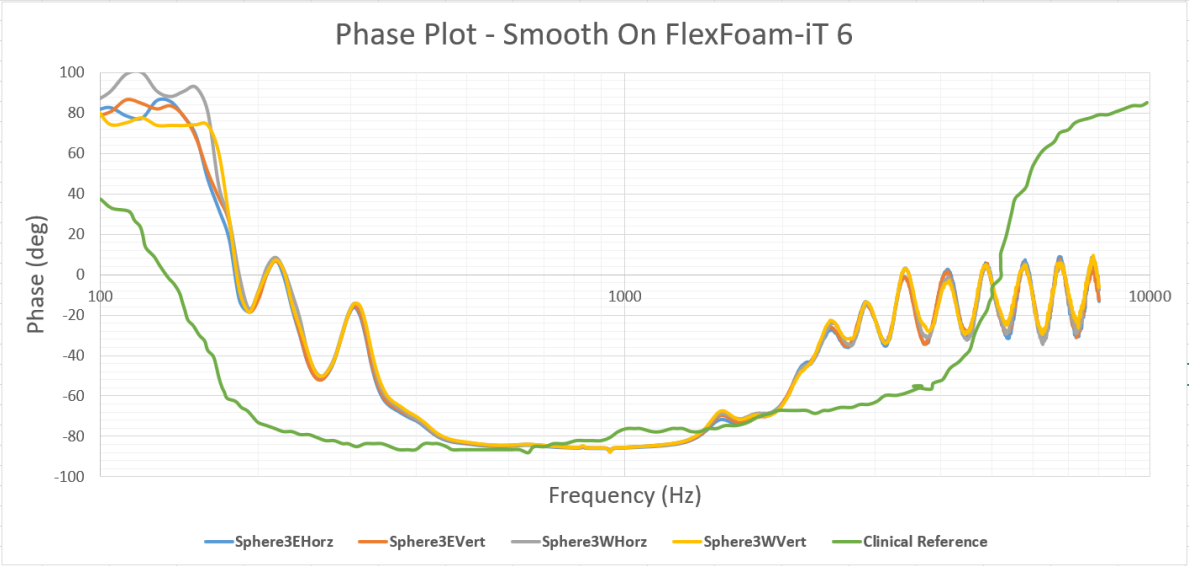

Figure 4.6: Phase plot for sphere 3 - Smooth On FlexFoam - iT™ 6.

4.4 Sphere 4 - Smooth On FlexFoam iT III™

4.4.1 Impedance Magnitude

The impedance magnitude plots for the sphere 4 which is filled with Smooth On FlexFoam - iT™ III, a variety of PUR, are shown in Figure 4.7. Here the CR are represented as a curve in green color. Sphere 4EHorz is shown in light blue color, sphere4EVert is represented in orange color, sphere 4WHorz is represented in grey color and finally the sphere4WVert is represented in yellow color. The frequency values in x-axis are represented in the logarithmic scale with its unit in hertz and the impedance magnitude has its units in decibels.

The impedance magnitude initially rises from 100 Hz and at these low frequencies, the response is purely mass controlled. Around 216 Hz, the first anti resonance peak is encountered with a maximum impedance magnitude of 78.8 dB. After this sharp peak, there is a decrease in impedance magnitude and hence we can say this region is under stiffness control. A shorter and smaller magnitude, second anti-resonance peak at 304 Hz is encountered with a magnitude of around 67 dB. There is an increase in magnitude from around 272 Hz till the second anti resonance peak. At these frequency regions, impedance response is mass controlled which again changes to stiffness controlled after the peak with decrease in impedance magnitude. This second anti resonance peak is highly undesirable and not compliant with the CR values.

The impedance response matches the CR from 500 Hz until 800 Hz. Post 800 Hz, there is significant deviation in impedance response in comparison with CR values and this region is still stiffness controlled with decreasing magnitude. Ripples start appearing at around 2312 Hz. This means that there is a continuous increase and decrease in the impedance magnitude at the region, thereby alternating between the mass and stiffness controlled regions. This ripple behaviour is undesirable and not in keeping with our CR values.The reasoning for these ripples is not yet known clearly and needs to be further investigated. This might be due to inherent nature of the material, damping, or even some issues with measurement such as rigid coupling, decoupling issues or insufficient mass/phase compensation. This ripple behavior continues in the high frequency region until 8000 Hz, again highly undesirable for our need.

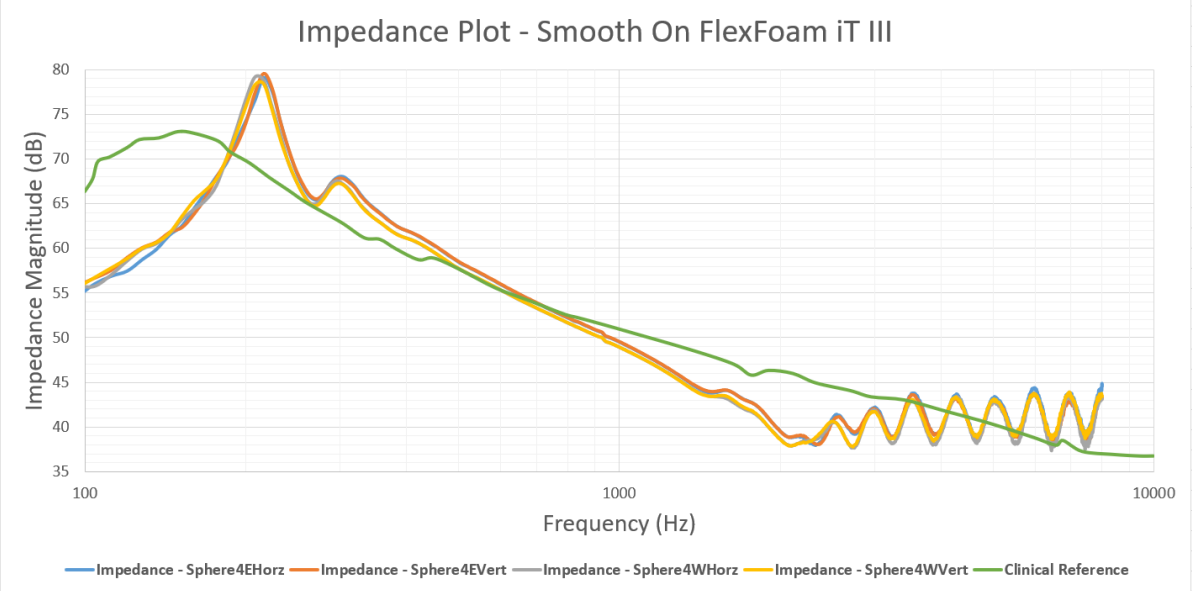

Figure 4.7: Impedance plot for sphere 4 - Smooth On FlexFoam iT™ III.

4.4.2 Phase Measurement

The phase plots for the sphere 4 which is filled with Smooth On FlexFoam - iT™ III, a variety of PUR, are shown in Figure 4.8. The same color markings are used here as shown in Figure 4.7. The frequency values in x-axis are represented in the logarithmic scale with its unit in hertz and the phase has its units in degrees.

At low frequencies, there is a positive phase close to 80-90 degrees. Around 216 Hz, a negative phase is encountered and the value decreases further. There are two peaks in the low frequency regions, with the second peak, starting at 248 Hz, being smaller in magnitude, as the curve decreases in phase value and enters negative phase. At mid frequencies over 416 Hz, the curve starts to flatten. At high frequencies around 2400 Hz, the curve increases in phase and ripples are introduced, which continues till 8000 Hz. At 8000 Hz, the phase difference between the plots and CR curve is around 93 degrees. Phase plot for sphere 4 does not match the CR values, as there is a vast difference between the plot and CR values.

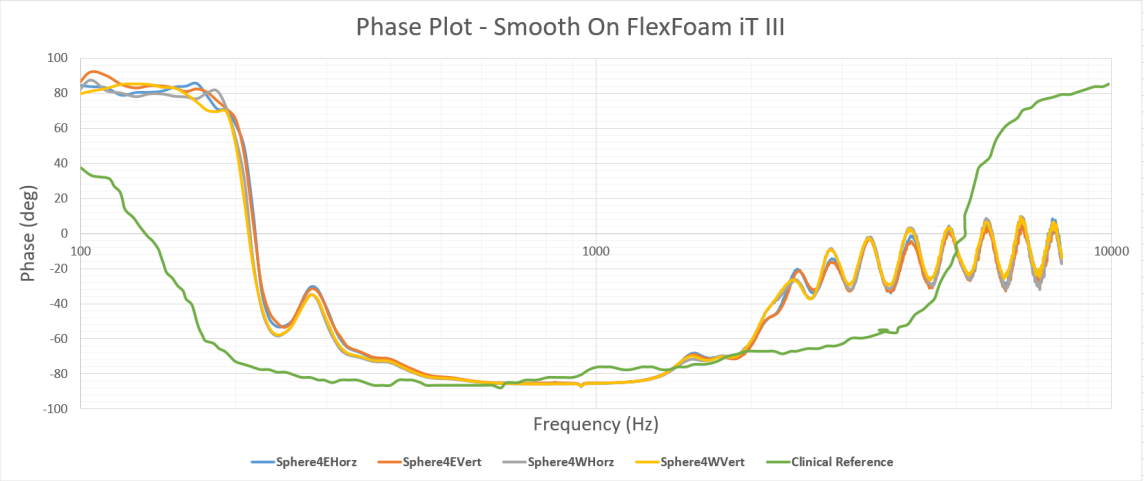

Figure 4.8: Phase plot for sphere 4 - Smooth On FlexFoam iT™ III

4.5 Sphere 5 - Hollow Sphere

4.5.1 Impedance Magnitude

The impedance magnitude plots for sphere 5 which is empty without the addition of any brain surrogate material are shown in Figure 4.9. Here the CR is represented as a curve in green color. Sphere 5EHorz is shown in light blue color, sphere5EVert is represented in orange color, sphere5WHorz is represented in grey color and finally the sphere 5WVert is represented in yellow color. The frequency values in x-axis are represented in the logarithmic scale with its unit in hertz and the impedance magnitude has its units in decibels.

The impedance magnitude initially rises from 100 Hz and at these low frequencies, the response is purely mass controlled. Around 288 Hz, the first anti resonance peak is encountered with a maximum impedance magnitude of 83 dB. After this peak, there is a decrease in impedance magnitude and hence this region is under stiffness control and represented as compliance instead of impedance.

Post 800 Hz, there is significant deviation in impedance response in comparison with CR values and this region is still stiffness controlled with decreasing magnitude. Ripples start appearing at around 1528 Hz. This means that there is a continuous increase and decrease in the impedance magnitude at the region, thereby alternating between the mass and stiffness controlled regions. This ripple behaviour is undesirable and not in keeping with our CR values. The reasoning for these ripples is not yet known clearly and needs to be further investigated. This might be due to inherent nature of the material, damping or even some issues with measurement such as rigid coupling, decoupling issues, or insufficient mass/phase compensation. This ripple behavior continues in the high frequency region until 8000 Hz, again highly undesirable for our need.

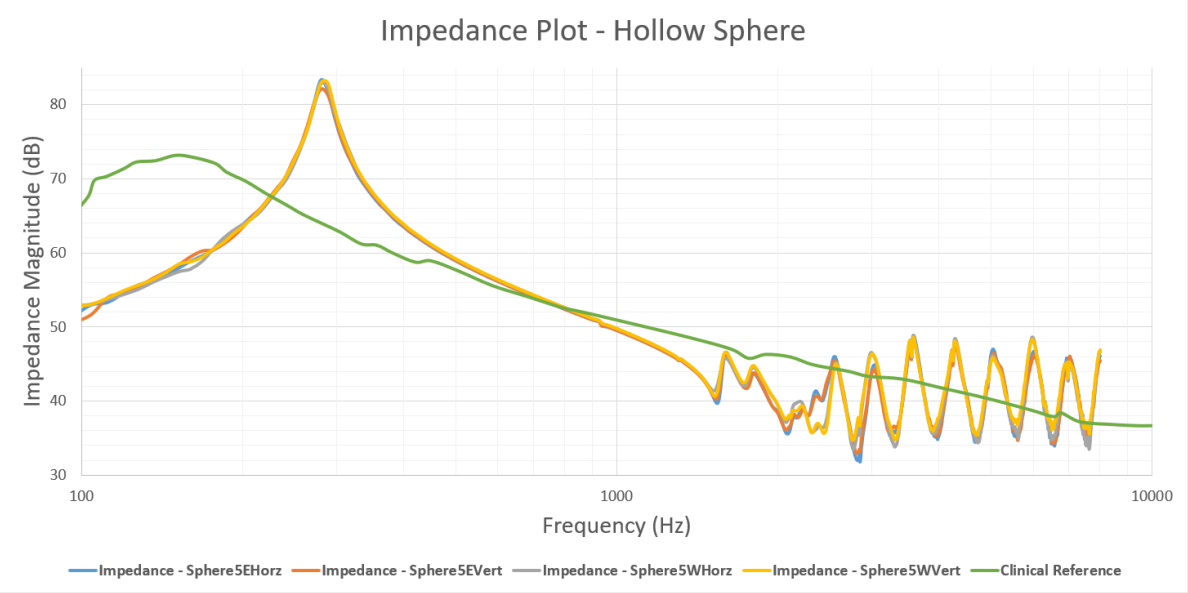

Figure 4.9: Impedance plot for sphere 5 - Hollow Sphere.

4.5.2 Phase Measurement

The phase plots for sphere 5 which is empty without the addition of any brain surrogate material are shown in Figure 4.10. The same color markings are used here as shown in Figure 4.9. The frequency values in x-axis are represented in the logarithmic scale with its unit in hertz and the phase has its units in degrees.

At low frequencies, there is a positive phase close to 80 degrees. Around 288 Hz, a negative phase is encountered and the value decreases further. At mid frequencies over 344 Hz, the curve starts to flatten. At high frequencies around 1568 Hz, the curve increases in phase and ripples are introduced. Phase plot for sphere 5 does not match the CR values, as there is a vast difference between the plot and CR values. At 8000 Hz, the phase difference between the plots and CR curve is around 88 degrees.

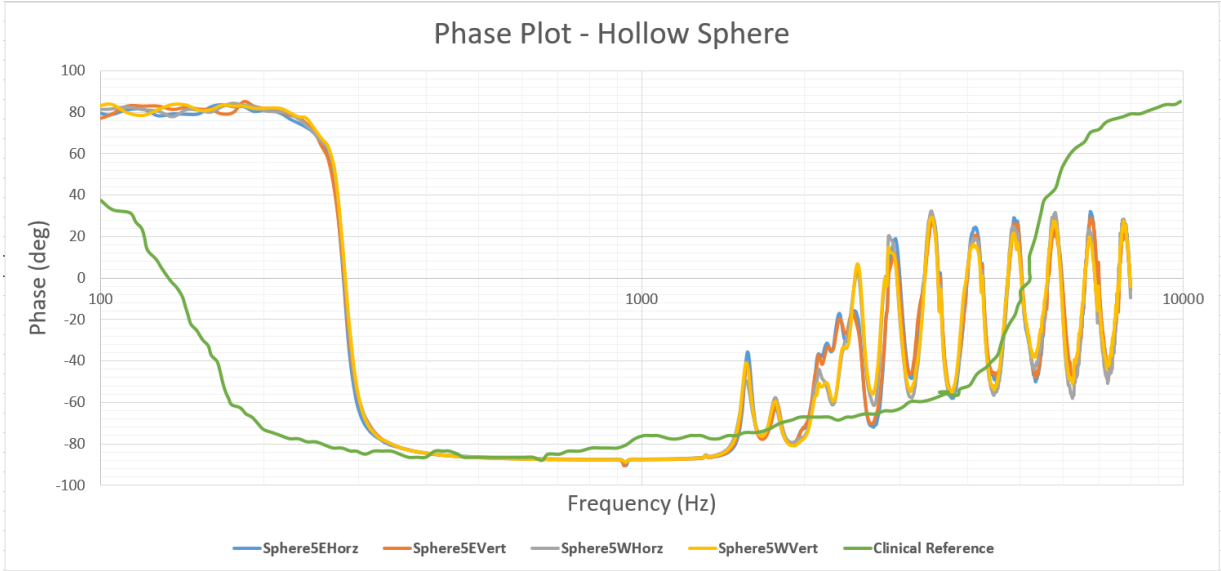

Figure 4.10: Phase plot for sphere 5 - Hollow sphere.

4.6 Sphere 6 - Permagel

4.6.1 Impedance Magnitude

The impedance magnitude plots for the sphere 6 which is filled with permagel, are shown in Figure 4.11. Here the CR is represented as a curve in green color, sphere6EHorz is shown in light blue color, sphere6EVert is represented in orange color, sphere6WHorz is represented in grey color, sphere6WVert is represented in yellow color. The frequency values in x-axis are represented in the logarithmic scale with its unit in hertz and the impedance magnitude has its units in decibels.

One observation for sphere 6 filled with permagel was that the permagel surrogate shrunk and reduced in volume with time. This shrinkage is mainly concentrated at the opening of the sphere and not at the measurement site on the sphere. I believe this shrinkage did not impact the readings in any way. The impedance magnitude initially rises from 100 Hz and at these low frequencies, the response is purely mass controlled and having a positive slope. Around 136 Hz, the first anti resonance peak is encountered with a maximum impedance magnitude of 86 dB. At this point, the impedance difference with the CR is around 10-12 dB. After this peak, there is a decrease in impedance magnitude and hence this negative slope is under stiffness control and represented as compliance (reciprocal of stiffness) instead of impedance. The impedance response however matches that of CR till around 630 Hz.

At middle frequencies from 630 Hz till 1664 Hz, mild ripples are introduced in the measurements. This means that there is a continuous increase and decrease in the impedance magnitude at the region, thereby alternating between the mass and stiffness controlled regions. This ripple behaviour is undesirable and not in keeping with our CR values, yet the ripples meet the CR values at various points. At high frequencies, the impedance response is close to the CR, but still, some deviation in the magnitudes, say around 4 dB, exists at 8000 Hz. However, there are not many ripples at high frequencies.

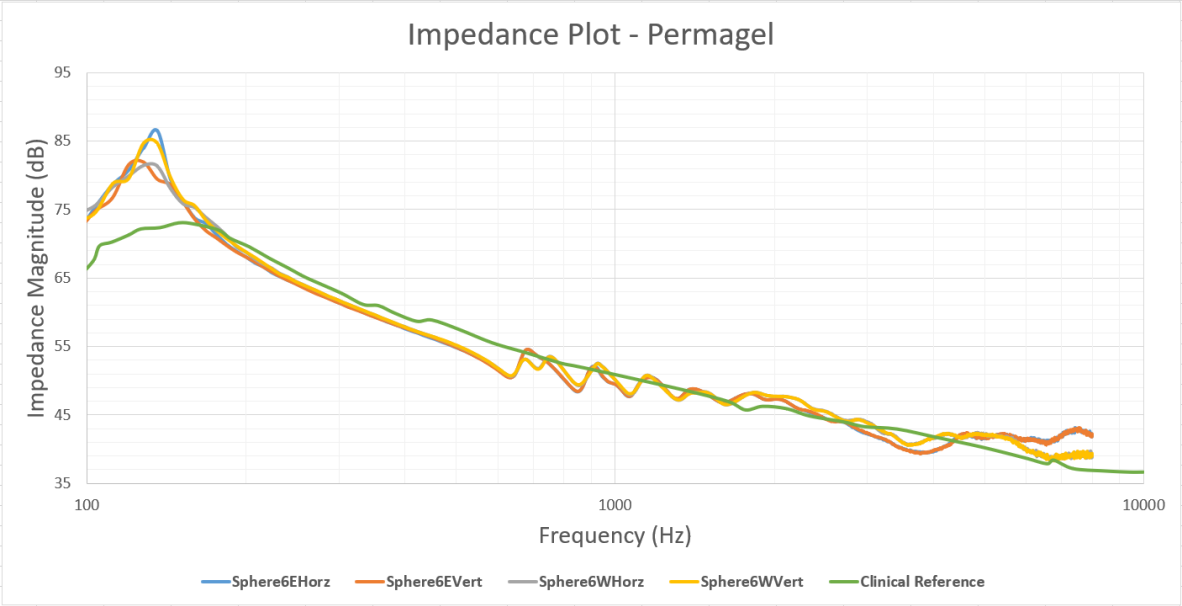

Figure 4.11: Impedance plot for sphere 6 - Permagel.

4.6.2 Phase Measurement

The phase plots for sphere 6 which is filled with permagel, are shown in Figure 4.12. The same color markings are used here as shown in Figure 4.3. The frequency values in x-axis are represented in the logarithmic scale with its unit in hertz and the phase has its units in degrees.

At low frequencies around 128 Hz, the plot enters into a negative phase and has a significant difference with CR values. At mid frequencies, starting from 610 Hz till 1890 Hz, ripples are introduced in the plots, mirroring the corresponding impedance magnitude response curve. At high frequencies over 3544 Hz, the curve increases in phase, but again drastically different from the CR curve. Phase plot for sphere 6 does not completely match the CR values. At 8000 Hz, the phase difference between the plots and CR curve is around 103 degrees

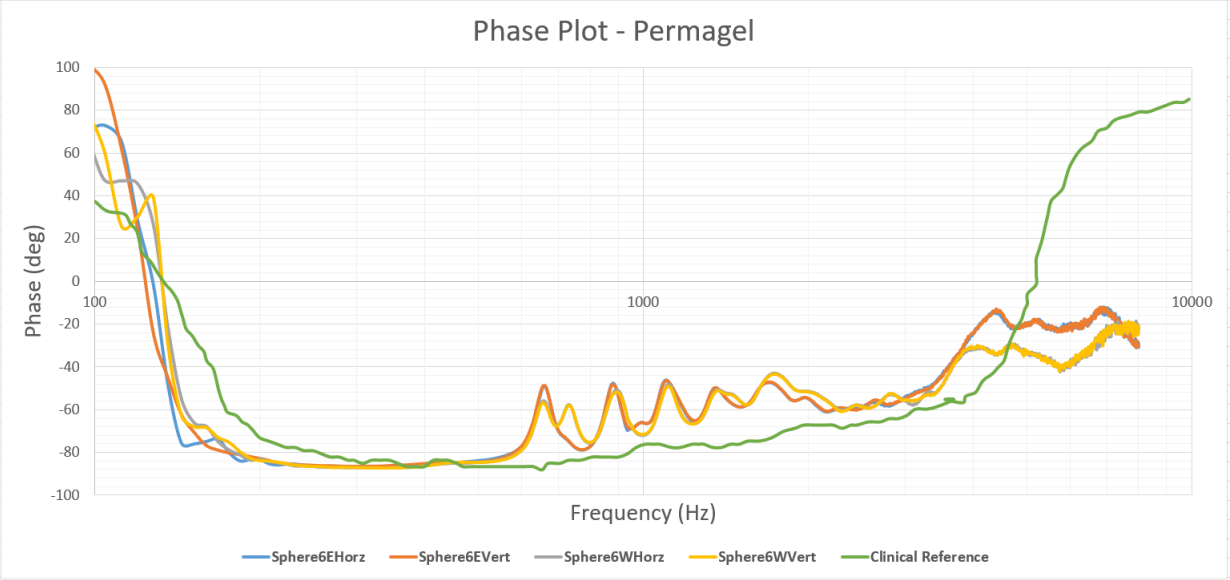

Figure 4.12: Phase plot for sphere 6 - Permagel.

4.7 Harald

4.7.1 Impedance Magnitude

The impedance magnitude plots for an existing artificial head at Cochlear -"Harald", have been shown in Figure 4.13. The CR values are represented as a curve in green color, the values from "HaraldWHorz" is represented through a light blue curve and the values from "HaraldWVert" is represented through an orange curve. The frequency values in x-axis are represented in the logarithmic scale with its unit in hertz and the impedance magnitude has its units in decibels.

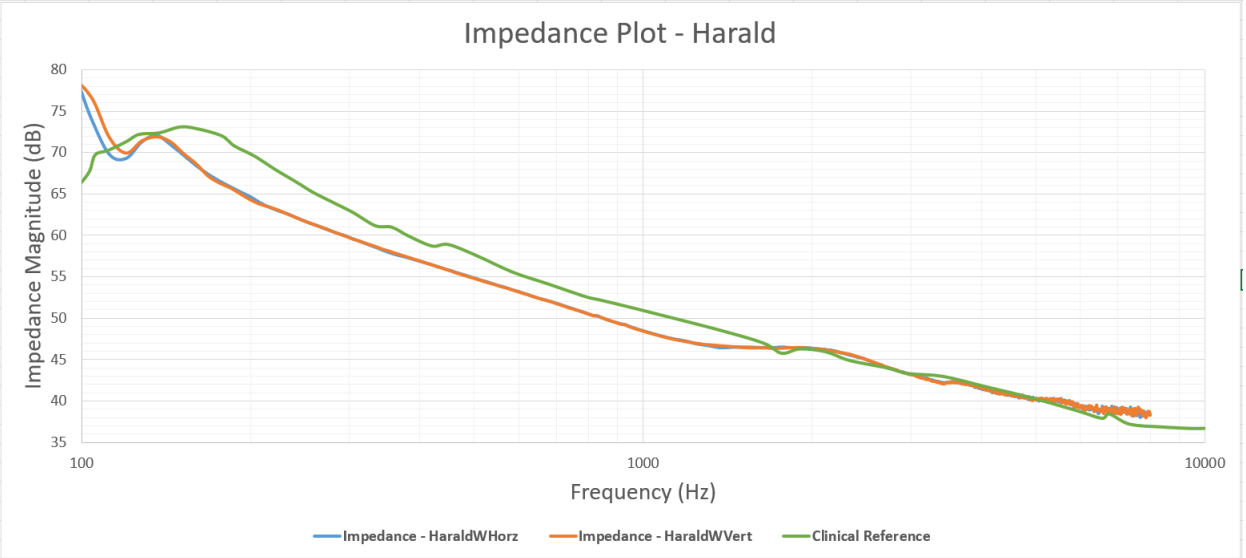

Figure 4.13: Impedance plot of Harald.

4.7.2 Phase Measurement

The phase plots for an existing artificial head at Cochlear -"Harald", have been shown in Figure 4.14. The same color markings are used here as shown in Figure 4.13. The frequency values in x-axis are represented in the logarithmic scale with its unit in hertz and the phase has its units in degrees.

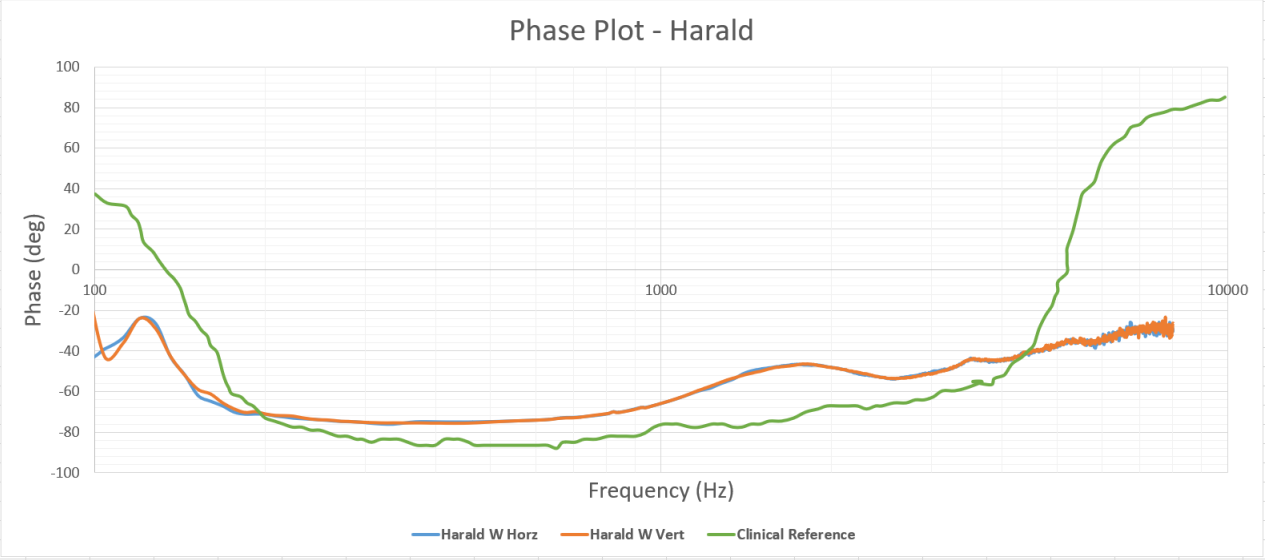

Figure 4.14: Phase plot of Harald.

5

Discussion

One assumption that needs to be made when it comes to interpreting the output of BCD, especially the skull impedance measurement is that skull impedance is linear. This means that one gets the same magnitude of impedance and phase irrespective of the force stimulation level. Preference was to use the median over average values for CR, as average includes the outliers, even though the actual difference between the median and average values is minimal. The frequency response is divided into three regions - low frequencies (100 to 300 Hz), mid frequencies (300 to 3000 Hz), high frequencies (3000 to 10000 Hz). From the plots of CR values, the impedance response is mass controlled till around 150 Hz, then it encounters a forced resonance called anti-resonance. After this peak, the impedance response becomes stiffness controlled and the impedance in this region is represented as compliance. Finally, at high frequencies, there is a transition back to being a pure mass from stiffness controlled region, as the main interaction at these high frequencies only involves the mass of the titanium implant and the surrounding bone.

Also, the measurements did not vary much when the readings were taken at west or east positions, where BI300 was implanted and the variability was minimal for the pillow decoupling oriented vertically or horizontally. Measurements were taken at various positions and orientations to ensure and reconfirm that they produce the same result when measured anywhere on the sphere irrespective of the pillow decoupling orientation or in simpler terms to ensure repeatability. Deviations between these readings are minuscule across all spheres and they are frequency dependant. Typically these deviations among these various orientations are 1-2 dB, with a maximum deviation of 5 dB observed in sphere 6 at its first anti resonance peak.

Anti-resonance peaks also called parallel resonance peaks, arise when the mass of the attachment (titanium screw osseointegrated with parietal bone) and the compliance of the system interacts, resulting in an impedance magnitude peak. This means that motions are drastically reduced at the attachment point owing to the drastic increase in impedance magnitude. The estimated maximum anti resonance peak, where it exhibits maximum magnitude of MPI is 4500 Ns/m at around 150 Hz [36]. Phase values are represented between +90 degrees and -90 degrees. Here +90 degrees represent pure mass response and -90 degrees represent pure spring response.

For our measurement, the connection of the transducer and impedance head with BI300 abutment through a snap coupling adaptor is quite a rigid connection. Also, a pillow has been used to provide decoupling. Both these situations are not ideal and the values below 100Hz need to be taken with a grain of salt i.e., quite unreliable measurements.

Illustration of the force vibrations on the skulls in frequency regions close to anti-resonance

frequency is illustrated in Figure 5.1, as described in Hakansson et al., [36]. At low frequencies, there is minimal movement in the lower part of the head, as it is closely attached to the neck and shoulders which leads to significant damping. However, at the ipsilateral side, where there is force excitation, the skull vibrates in a to and fro manner. A similar response is observed at the contralateral side as well. At anti-resonance, vibration at the ipsilateral stimulation side is not possible due to an anti-resonance peak while the contralateral side vibrates. Beyond anti-resonance frequency, it is compliance controlled with light damping. High frequencies are characterized by force on titanium implant and the surrounding bone. Hence it becomes mass controlled again and vibrations at the ipsilateral side are observed, while no motion could be witnessed at the contralateral side [36].

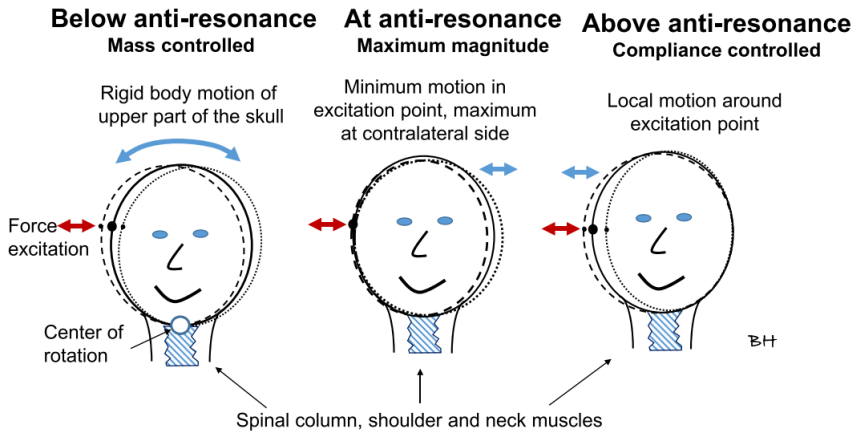

Figure 5.1: Illustration of impedance response of skulls at below, at and above anti-resonant frequency ≈ 150 Hz. [36]

5.1 Final Result

5.1.1 Impedance Magnitude

The final collection of impedance magnitude plots are shown in Figure 5.2. Each sphere's values in different positions and orientations are averaged and presented here for ease of comparison. Here the CR is shown as dots in black color. The final plots of synthetic gelatin (light blue), Smooth-On FlexFoam - iT™ 14 (orange), Smooth-On FlexFoam - iT™ 6 (grey), Smooth-On FlexFoam - iT™ III (yellow), hollow sphere (purple), permagel (green), harald (red) and CR (brown) are represented. The frequency values in x-axis are shown in the logarithmic scale with its unit in hertz and the impedance magnitude has its units in decibels.

From the Figure 5.2, it is inferred that the existing head simulator - Harald is the closest match with the CR values for MPI, but they do have some inherent drawbacks such as variability with time, degradation due to microbial contamination, etc. Finding alternatives for the existing system is what this whole thesis project is about. The first anti-resonance peak is common and normal due to the forced resonance phenomenon when a sufficient force input of vibrations strikes the temporal or parietal bone in the skull from the sound processor attached to the osseointegrated implant.

Sphere 1 with synthetic gelatin has varying impedance magnitude at the site of anti resonance peak but its magnitude decreases after the peak and starts to match the clinical impedance from around 200 Hz till 500 Hz. Post 500 Hz, ripples are introduced at mid frequencies, which are undesirable. These ripples end at 1500 Hz and the high frequency response is close to the CR values, even though there is a minor discrepancy with the impedance values of the order of 5dB at 8000 Hz. In short, Sphere 1 has moderately comparable low and high frequency responses, but the mid frequencies are affected by ripple formation. Sphere 1 having its first anti resonance peak at 128 Hz is a concern since clinical studies estimate it to be around 145-150 Hz [36][40][38].

Spheres 2,3 and 4 which are all made up of different PUR foams, show some similarity when it comes to their impedance response. Spheres 2 and 4 have a second anti-resonance peak while sphere 3 has both second and third anti-resonance peaks. These second and third anti resonance peaks are undesirable. All the three sphere's impedance values match the CR in the frequency range of 500-800 Hz. Post 800 Hz, there is a large deviation and ripples start to appear at high frequencies. Sphere 5, which is just a hollow sphere, shows massive deviation during the first anti-resonant peak. The impedance value matches with CR for a limited frequency bandwidth of 650-1000 Hz. Again after 1500, ripples start to appear and high frequencies are completely affected by ripples.

Sphere 6 filled with permagel seems to be the best fit of the materials tested. It has its first anti resonance peak at 136 Hz, much closer to the clinical standard of 145 Hz. Also, the impedance difference at this anti resonance peak is 10-12 dB. It matches the CR after this point, even though mild ripples are introduced at mid frequencies 630 to 1664 Hz. Post this frequency the curve becomes smooth and closely matches the CR values at high frequencies until encountering a minor 4 dB magnitude difference at 8000 Hz. Even though there was shrinkage of few centimeters noticed in the head after few weeks, it is

mostly close to the opening and not close to the measurement site. Hence the chances of this shrinkage affecting the reading are very slim or minimal.

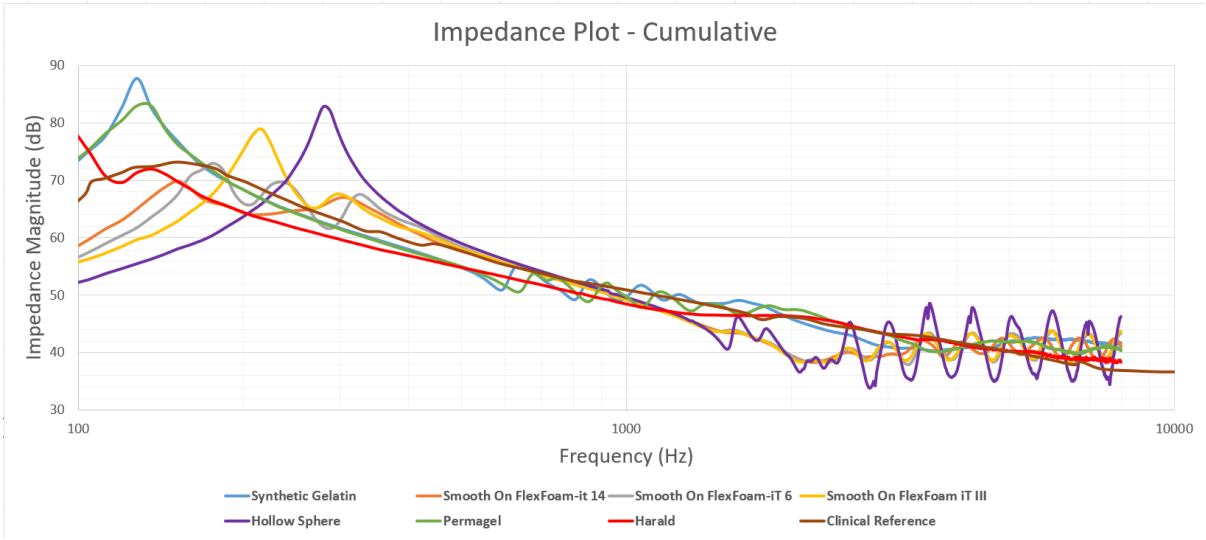

Figure 5.2: Final Magnitude Plot.

5.1.2 Phase Measurement

The final collection of phase plots is shown in Figure 5.3. The same color markings are used here as shown in Figure 5.2. The frequency values in x-axis are shown in the logarithmic scale with its unit in hertz and the phase has its units in degrees.

When it comes to phase plots, none of the heads tested or even the existing artificial head Harald could match the CR values. Apart from Harald, all the spheres start with a positive phase at 100 Hz, signifying a mass-controlled response very much like our CR. Then the curve enters the negative phase and becomes spring controlled. At mid frequencies from 300 Hz till 650, Spheres 2-5 have a close correspondence with CR, as the curves start to flatten. Sphere 1 and Sphere 6, experience ripples at mid frequencies and there is a significant deviation from CR. Post 650 Hz, the CR starts to rise and begins to be mass controlled again. It reaches a maximum of 80 deg at 8000 Hz. All the spheres also begin to get mass controlled post 1300 Hz. Except for synthetic gelatin and permagel, ripples are experienced at high frequencies. Harald does not closely correlate and correspond to any of the curves. There exist a significant phase difference for the CR with the other curves at 8000 Hz and beyond.

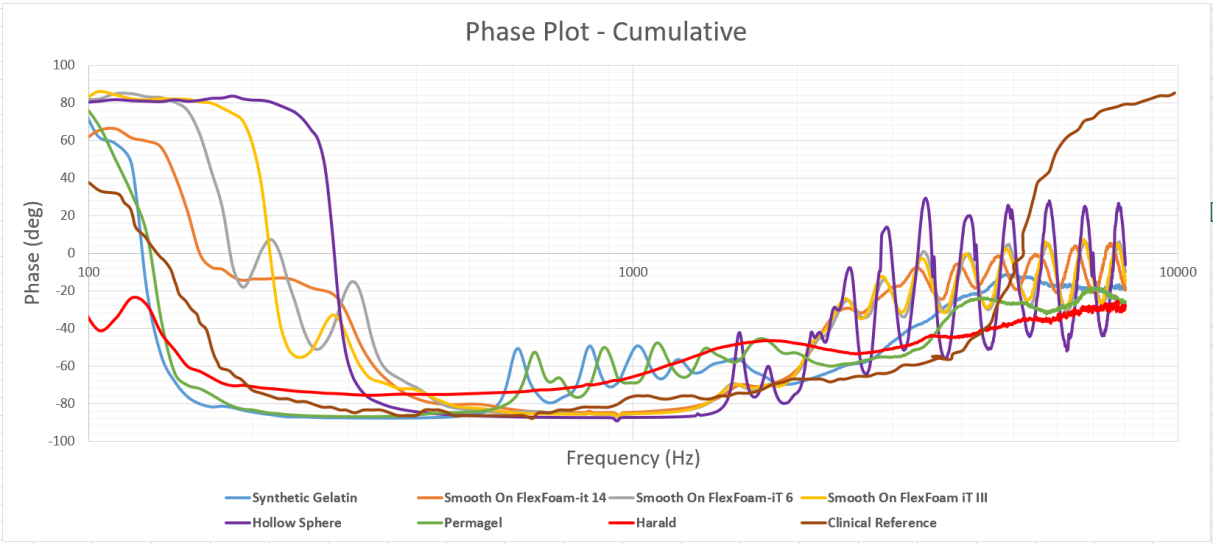

Figure 5.3: Final Phase Plot.

5.2 Comparison of Permagel Head with Dry Skull, Head, FEM

The mechanical impedance results obtained in sphere 6, i.e., Permagel head are compared with previous studies which measured MPI on dry skulls [75], head [76] and FEM simulation [55] are represented in the figure 5.4. Here the permagel head results are shown in the plot as a light blue color curve, existing head simulator "Harald" in an orange color curve, clinical reference as a grey curve, dry skull as a yellow curve, FEM as a dark blue curve, and the head investigated by Stefan and Goode in a green color curve. The frequency values in x-axis are shown in the logarithmic scale with its unit in hertz and the phase has its units in degrees.

Permagel head (sphere 6) has been identified as the best fit among the brain surrogate materials considered. Hence this Permagel has been compared with related experimental studies measuring MPI values - dry skull/cadaver by Stenfelt et al. [75], head by Stenfelt and Goode [76], FEM by Chang et al. [55], and the CR and harald values have been included in the plots for further reference as shown in Figure 5.4. The impedance response of optimized FEM and cadaver follows a similar pattern.

Cadaver has its first anti resonance peak at 126 Hz with a magnitude of 54 dB. Then it becomes stiffness controlled before encountering a second anti-resonance peak at 177 Hz and 59 dB. At 550 Hz it reaches its highest peak with a magnitude of 79 dB. Then the slope decreases with stiffness behavior. Ripples are encountered between 1250 Hz and 3590 Hz. The optimized FEM matches the impedance response of the cadaver, mainly through its highest peak, which happens to be its first anti resonance peak with a frequency of 603 Hz and a magnitude of 81 dB. Ripples start appearing around 993 Hz and the same pattern continues until high frequencies. However, the high frequency response is still quite close to that of the cadaver. Head, which was experimented with by Stenfelt and Goode [76], has its first anti-resonance peak at 250 Hz and impedance magnitude of 70 dB. Post this frequency it has a stiffness controlled response and a decreasing slope. After 1000 Hz, the impedance response is close to that of the cadaver and FEM.

Now the remaining curves - permagel, harald, and CR, whose impedance responses were discussed in previous sections. These three curves show a close correlation and a similar pattern. The main discrepancy for the permagel head is that nearly ten dB variation exists at the first anti resonance peak in comparison with CR and harald. Both permagel and harald reach their first anti-resonance peak at 136-137 Hz, which is a bit early than that of CR. Ripples encountered by permagel at mid frequencies are a concern. Overall these three curves show a close correlation and a similar pattern. A significant difference exists between permagel head impedance response in comparison with earlier studies and experiments on the dry skull, head, and optimized FEM.

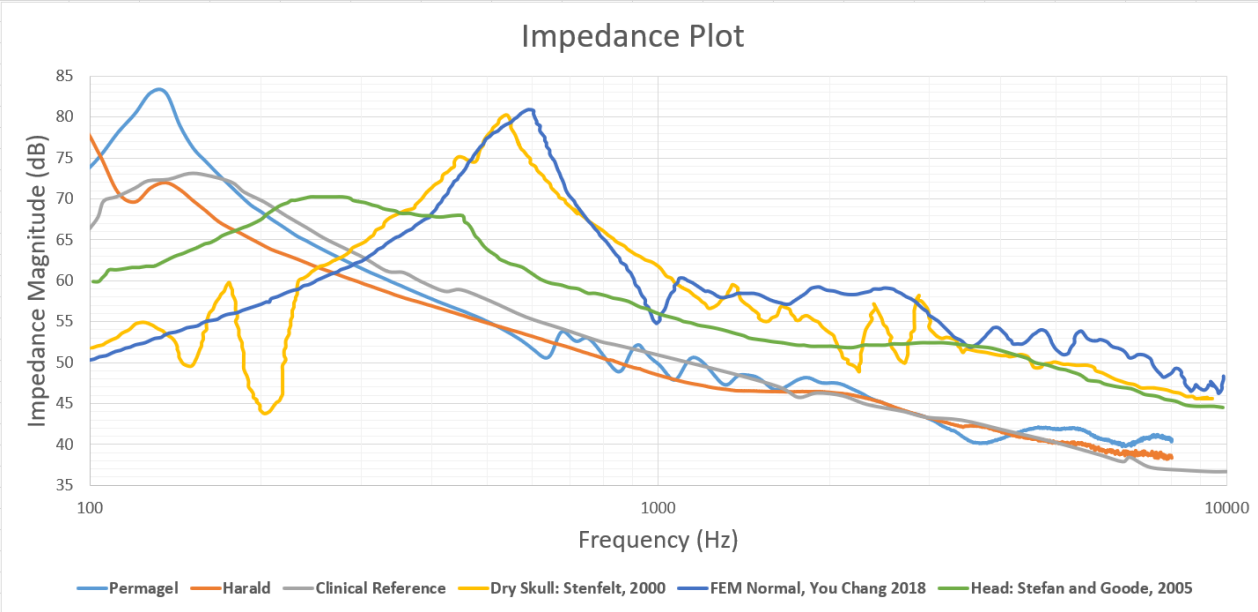

Figure 5.4: Comparison of Permagel head with dry skull, head, FEM. [75][55][76]

6

Conclusion

After a comprehensive analysis of the impedance magnitude plots, Sphere 6 with permagel is the best option among the six spheres considered. Permagel filled sphere has its anti-resonance frequency at 136 Hz, which is the closest among the surrogates considered, to the CR value of 145-150 Hz. Also, the impedance magnitude at anti-resonance frequency varies with the corresponding CR of the order 10-12 dB. The frequency dependence of MPI is quite comparable with CR, even if there are deviations of few decibels. Ripples encountered at mid frequencies are quite undesirable and uncharacteristic with CR. At high frequencies, ripples are minimal and closely correspond with CR. Overall, it's similar in pattern but not an exact match.

Sphere 1 is also suitable, however, it suffers from certain issues. Its initial anti-resonance peak magnitude varies with that of CR and also suffers from ripples at mid frequencies. In fact, synthetic gelatin is quite comparable with permagel in its impedance response, but Permagel is the better option among the two, owing to reduced ripples at mid frequencies, close correspondence with CR at low and high frequencies. Other spheres - 2, 3, 4, and 5 are unsuitable as they have either undesirable second and third anti resonance peaks, massive deviations post 1000 Hz, and continuous ripples at high frequencies. None of the heads tested have an exact phase response as compared to the CR values. The general CR phase plot trend is similar to the heads tested at low and mid frequencies, but not at high frequencies. It would be interesting to test permagel as a brain surrogate on an anatomically correct head, which will be the next stage of this project/study to be conducted at a future date. The conclusion is that permagel could potentially mimic brain properties, however, it is not a perfect substitute with an exact match of CR impedance and phase values.

However, it must be noted that the ideal brain surrogate material could only be finalized after performing a transcranial attenuation test, and comparing it with CR values. Also the results might change if it is to be tested on artificial anatomically correct skulls. These two factors must be taken into consideration as well.

7
Future Work

Synthetic gelatin used here was specifically made to mimic the human brain. When the package was received, the material was a bit soft and skepticism existed about its ability to handle damping. There are however other versions of the same synthetic gelatin with differing additives. Those could be investigated and the potential exists for a solution. The impedance measurement setup could be improved without a rigid connection of an adapter or snap coupling with the BI300 implant. Also, the decoupling could be improved. Mass and phase compensation is approximate and not exactly accurate.

After identification of the ideal surrogate material, which this study suggests as Permagel, it needs to be cast on commercially available anatomically correct skulls. Only mechanical impedance measurement was possible with this study owing to time constraints. It would be interesting to test these spheres for other parameters such as TA and AF. Based on all these test results, an ideal brain surrogate material could be identified. An anatomically correct skull could be developed in the future, building upon this thesis work.

If there exists a higher budget, usage of 3D printing or additive manufacturing for skulls/ skin could be considered. Another challenge is to account for variability in the mechanical/acoustical properties of various bones of the human skull and to document the MPI values for different skull bones.

Bibliography

[1] C. J. Freitas, J. T. Mathis, S. Nikki, R. P. Bigger, and J. Mackiewicz, "Dynamic response due to behind helmet blunt trauma measured with a human head surrogate. int j med sci. 2014 mar 8;11(5):409-25. doi: 10.7150/ijms.8079. pmid: 24688303; pmcid: Pmc3970092.," *Int J Med Sci.*, 2014. [Online]. Available: `https://pubmed.ncbi.nlm.nih.gov/24688303/` (visited on 11/30/2020).

[2] P. Mahoney, D. Carr, R. Delaney, N. Hunt, S. Harrison, J. Breeze, and I. Gibb, "Does preliminary optimisation of an anatomically correct skull-brain model using simple simulants produce clinically realistic ballistic injury fracture patterns? int j legal med. 2017 jul;131(4):1043-1053. doi: 10.1007/s00414-017-1557-y. epub 2017 mar 7. pmid: 28271364; pmcid: Pmc5491591.," *Int J Legal Med.*, 2017. [Online]. Available: `https://pubmed.ncbi.nlm.nih.gov/28271364/` (visited on 11/30/2020).

[3] P. Mahoney, D. Carr, R. Arm, I. Gibb, N. Hunt, and R. J. Delaney, "Ballistic impacts on an anatomically correct synthetic skull with a surrogate skin/soft tissue layer. int j legal med. 2018 mar;132(2):519-530. doi: 10.1007/s00414-017-1737-9. epub 2017 nov 28. pmid: 29185026; pmcid: Pmc5807523.," *Int J Legal Med.*, 2018. [Online]. Available: `https://pubmed.ncbi.nlm.nih.gov/29185026/` (visited on 12/03/2020).

[4] S. Sutar and G. Shailesh, "Investigation of wave propagation through head layers with focus on understanding blast wave transmission. biomech model mechanobiol. 2020 jun;19(3):875-892. doi: 10.1007/s10237-019-01256-9. epub 2019 nov 19. pmid: 31745681.," *Biomechanics and Modeling in Mechanobiology*, 2020. [Online]. Available: `https://pubmed.ncbi.nlm.nih.gov/31745681/` (visited on 12/03/2020).

[5] M. J. Thali, B. P. Kneubuehl, and R. Dirnhofer, "A "skin-skull-brain model" for the biomechanical reconstruction of blunt forces to the human head. forensic sci int. 2002 feb 18;125(2-3):195-200. doi: 10.1016/s0379-0738(01)00639-9. pmid: 11909663.," *Elsevier: Forensic Science International*, 2001. [Online]. Available: `https://pubmed.ncbi.nlm.nih.gov/11909663/` (visited on 12/03/2020).

[6] M. J. Thali, B. P. Kneubuehl, U. Zollinger, and R. Dirnhofer, "The "skin-skull-brain model": A new instrument for the study of gunshot effects. forensic sci int. 2002 feb 18;125(2-3):178-89. doi: 10.1016/s0379-0738(01)00637-5. pmid: 11909661," *Elsevier: Forensic Science International*, 2001. [Online]. Available: `https://pubmed.ncbi.nlm.nih.gov/11909661/` (visited on 12/03/2020).

[7] G. J. Tortora and B. Derrickson, "Introduction of the human body - the essentials of anatomy and physiology," *8th edition, John Wiley and Sons Inc.*, no. May, pp. 314–321, 2021.

[8] C. Rigato, "On direct drive bone conduction devices," *Doctoral Thesis - Chalmers University of Technology*, 2019. [Online]. Available: `https://research.chalmers.se/publication/509257/file/509257_Fulltext.pdf` (visited on 04/04/2021).

[9] *Anatomy of the human ear.* https://upload.wikimedia.org/wikipedia/commons/d/d2/Anatomy{_}of{_}the{_}Human{_}Ear.svg, Accessed: 2021-04-02.

[10] R. Carhat, "Clinical application of bone conduction audiometry. arch otolaryngol. 1950 jun;51(6):798-808. doi: 10.1001/archotol.1950.00700020824003. pmid: 15419943.," *Arch Otolaryngol. 1950 Jun;51(6):798-808.*, 1950. [Online]. Available: https://pubmed.ncbi.nlm.nih.gov/15419943/ (visited on 05/04/2021).

[11] P. J. Antonelli, "An overview of hearing loss.," *UFHealth*, 2002. [Online]. Available: http://www.ent.ufl.edu/files/conditions/hearing_loss_9_04.pdf (visited on 04/05/2021).

[12] *Skull anatomy*, https://www.britannica.com/science/osteoclast, Accessed: 2021-04-02.

[13] *Teach me anatomy - bones of the skull*, https://teachmeanatomy.info/head/osteology/skull/, Accessed: 2021-05-01.

[14] H. Yousef, M. Alhajj, and S. Sharma, "Anatomy, skin (integument), epidermis. 2020 jul 27. in: Statpearls [internet]. treasure island (fl): Statpearls publishing; 2021 jan–. pmid: 29262154.," *StatPearls Publishing*, 2020. [Online]. Available: https://pubmed.ncbi.nlm.nih.gov/29262154/ (visited on 05/01/2021).

[15] J. A. McGrath and J. Uitto, "Anatomy and organization of human skin (2010). in rook's textbook of dermatology (eds t. burns, s. breathnach, n. cox and c. griffiths). https://doi.org/10.1002/9781444317633.ch3," *Textbook of Dermatology*, 2010. [Online]. Available: https://onlinelibrary.wiley.com/doi/10.1002/9781444317633.ch3 (visited on 05/01/2021).

[16] *Human skin anatomy*, https://www.123rf.com/photo_106706087_stock-vector-human-body-skin-anatomy-vector-illustration-with-parts-vein-artery-hair-sweat-gland-epidermis-dermis.html, Accessed: 2021-04-02.

[17] *Mayfield - brain and spine - anatomy of the brain*, https://mayfieldclinic.com/pe-anatbrain.htm, Accessed: 2021-05-01.

[18] *The anatomy of the human brain*, https://www.news-medical.net/health/The-Anatomy-of-the-Human-Brain.aspx, Accessed: 2021-05-01.

[19] P. Henry and T. Letowski, "Bone conduction: Anatomy, physiology, and communication," *Technical report, DTIC document*, 2007. [Online]. Available: https://www.researchgate.net/publication/257128890_Bone_conduction_Anatomy_physiology_and_communication (visited on 04/05/2021).

[20] S. Reinfeldt, "
bone conduction hearing in human communication sensitivity, transmission and applications", thesis for the degree of doctor of philosophy, chalmers university of technology, 2009, p. 3.," *Doctoral Thesis - Chalmers University of Technology,*, 2009. [Online]. Available: https://research.chalmers.se/en/publication/93679 (visited on 04/02/2021).

[21] S. Stenfelt, "
acoustic and physiologic aspects of bone conduction hearing, in implantable bone conduction hearing aids", ser. advances in oto-rhinolaryngology. karger, 2011, vol. 71, no. 71, pp. 10–21.," *Advances in Oto-RhinoLaryngology.*, 2011. [Online]. Available: https://pubmed.ncbi.nlm.nih.gov/21389700/ (visited on 04/02/2021).

[22] S. Reinfeldt, B. Håkansson, H. Taghavi, and M. Eeg-Olofsson, "New developments in bone-conduction hearing implants: A review. med devices (auckl). 2015 jan 16;8:79-93. doi: 10.2147/mder.s39691. pmid: 25653565; pmcid: Pmc4303401.," *Med Devices*

(Auckl), 2015. [Online]. Available: https://pubmed.ncbi.nlm.nih.gov/25653565/ (visited on 04/02/2021).

[23] H. Taghavi, "A novel bone conduction implant system," *Licentiate thesis - Chalmers University of Technology*, 2012. [Online]. Available: https://research.chalmers.se/en/publication/155547 (visited on 04/02/2021).

[24] B. Håkansson, A. Tjellström, U. Rosenhall, and P. Carlsson, "The bone-anchored hearing aid. principal design and a psychoacoustical evaluation. acta otolaryngol. 1985 sep-oct;100(3-4):229-39. doi: 10.3109/00016488509104785. pmid: 4061073.," *Acta Otolaryngol.*, 1985. [Online]. Available: https://pubmed.ncbi.nlm.nih.gov/4061073/ (visited on 04/05/2021).

[25] B. Håkansson, G. Lidén, A. Tjellström, A. Ringdahl, M. Jacobsson, P. Carlsson, and B. E. Erlandson, "Ten years of experience with the swedish bone-anchored hearing system. ann otol rhinol laryngol suppl. 1990 oct;151:1-16. doi: 10.1177/0003489490099-s1001. pmid: 2121086.," *Ann Otol Rhinol Laryngol Suppl.*, 1990. [Online]. Available: https://pubmed.ncbi.nlm.nih.gov/2121086/ (visited on 04/05/2021).

[26] A. Tjellström, B. Håkansson, and G. Granström, "Bone-anchored hearing aids: Current status in adults and children. otolaryngol clin north am. 2001 apr;34(2):337-64. doi: 10.1016/s0030-6665(05)70335-2. pmid: 11382574.," *Otolaryngol Clin North Am.*, 2001. [Online]. Available: https://pubmed.ncbi.nlm.nih.gov/11382574/ (visited on 04/05/2021).

[27] *Cochlear - baha connect system*, https://www.cochlear.com/us/es/home/products-and-accessories/baha-system/baha-implants/baha-connect-system, Accessed: 2021-04-02.

[28] A. Arnold, M.-D. Caversaccio, and A. Mudry, "Surgery for the bone-anchored hearing aid. adv otorhinolaryngol. 2011;71:47-55. doi: 10.1159/000323579. epub 2011 mar 8. pmid: 21389704.," *Adv Otorhinolaryngol.*, 2011. [Online]. Available: https://pubmed.ncbi.nlm.nih.gov/21389704/ (visited on 04/02/2021).

[29] H. Taghavi, B. Håkansson, S. Reinfeldt, M. Eeg-Olofsson, K.-J. Freden Jansson, E. Håkansson, and B. Nasri, "Technical design of a new bone conduction implant (bci) system. int j audiol. 2015;54(10):736-44. doi: 10.3109/14992027.2015.1051665. epub 2015 jun 12. pmid: 26068536.," *Int J Audiol.*, 2015. [Online]. Available: https://pubmed.ncbi.nlm.nih.gov/26068536/ (visited on 04/05/2021).

[30] B. Håkansson, "The balanced electromagnetic separation transducer a new bone conduction transducer. j acoust soc am. 2003 feb;113(2):818-25. doi: 10.1121/1.1536633. pmid: 12597176.," *J Acoust Soc Am.*, 2003. [Online]. Available: https://pubmed.ncbi.nlm.nih.gov/12597176/ (visited on 04/05/2021).

[31] K. J. F. Jansson, B. Håkansson, S. Reinfeldt, C. Rigato, and M. Eeg-Olofsson, "Magnetic resonance imaging investigation of the bone conduction implant - a pilot study at 1.5 tesla. med devices (auckl). 2015 oct 23;8:413-23. doi: 10.2147/mder.s90704. pmid: 26604836; pmcid: Pmc4629964.," *Med Devices (Auckl).*, 2015. [Online]. Available: https://pubmed.ncbi.nlm.nih.gov/26604836/ (visited on 04/05/2021).

[32] K. J. Jansson, B. Håkansson, S. Reinfeldt, H. Taghavi, and M. Eeg-Olofsson, "Mri induced torque and demagnetization in retention magnets for a bone conduction implant. ieee trans biomed eng. 2014 jun;61(6):1887-93. doi: 10.1109/tbme.2014.2309978. pmid: 24845299.," *n retention magnets for a bone conduction implant.*, 2014. [Online]. Available: https://pubmed.ncbi.nlm.nih.gov/24845299/ (visited on 04/05/2021).

[33] B. Håkansson, M. Eeg-Olofsson, S. Reinfeldt, S. Stenfelt, and G. Granström, "Percutaneous versus transcutaneous bone conduction implant system: A feasibility study on a cadaver head. otol neurotol. 2008 dec;29(8):1132-9. doi: 10.1097/mao.0b013e3181-6fdc90. pmid: 18769364.," *Otol Neurotol.*, 2008. [Online]. Available: https://pubmed.ncbi.nlm.nih.gov/18769364/ (visited on 04/05/2021).

[34] H. Taghavi, B. Håkansson, and S. Reinfeldt, "Analysis and design of rf power and data link using amplitude modulation of class-e for a novel bone conduction implant. ieee trans biomed eng. 2012 nov;59(11):3050-9. doi: 10.1109/tbme.2012.2213252. epub 2012 aug 15. pmid: 22907959.," *IEEE Trans Biomed Eng.*, 2012. [Online]. Available: https://pubmed.ncbi.nlm.nih.gov/22907959/ (visited on 04/05/2021).

[35] B. Håkansson, A. Tjellström, and U. Rosenhall, "Hearing thresholds with direct bone conduction versus conventional bone conduction. scand audiol. 1984;13(1):3-13. doi: 10.3109/01050398409076252. pmid: 6719012.," *Scand Audiol.*, 1984. [Online]. Available: https://pubmed.ncbi.nlm.nih.gov/6719012/ (visited on 04/05/2021).

[36] B. Håkansson, F. Woelflin, A. Tjellström, and W. Hodgetts, "The mechanical impedance of the human skull via direct bone conduction implants. med devices (auckl). 2020 sep 24;13:293-313. doi: 10.2147/mder.s260732. pmid: 33061679; pmcid: Pmc7522424.," *Med Devices (Auckl).*, 2020. [Online]. Available: https://pubmed.ncbi.nlm.nih.gov/33061679/ (visited on 03/13/2021).

[37] *Bruel and kjaer - artificial mastoid*, https://www.bksv.com/en/transducers/simulators/ear-mouth-simulators/artificial-mastoid-4930, Accessed: 2021-04-04.

[38] F. Woelflin, "Mechanical point impedance of skin penetrated human skull in vivo," *Master thesis - Chalmers*, 2011. [Online]. Available: https://odr.chalmers.se/handle/20.500.12380/143059 (visited on 03/14/2021).

[39] B. Håkansson and P. Carlsson, "Skull simulator for direct bone conduction hearing devices. scand audiol. 1989;18(2):91-8. doi: 10.3109/01050398909070728. pmid: 2756338.," *Scand Audiol.*, 1989. [Online]. Available: https://pubmed.ncbi.nlm.nih.gov/2756338/ (visited on 04/04/2021).

[40] B. Håkansson, P. Carlsson, and A. Tjellström, "The mechanical point impedance of the human head, with and without skin penetration. j acoust soc am. 1986 oct;80(4):1065-75. doi: 10.1121/1.393848. pmid: 3771927.," *J Acoust Soc Am.*, 1986. [Online]. Available: https://pubmed.ncbi.nlm.nih.gov/3771927/ (visited on 03/13/2021).

[41] S. Stenfelt, "Transcranial attenuation of bone-conducted sound when stimulation is at the mastoid and at the bone conduction hearing aid position. otol neurotol. 2012 feb;33(2):105-14. doi: 10.1097/mao.0b013e31823e28ab. pmid: 22193619.," *Otol Neurotol.*, 2012. [Online]. Available: https://pubmed.ncbi.nlm.nih.gov/22193619/ (visited on 03/19/2021).

[42] G. A. Studebaker, "Clinical masking of air- and bone-conducted stimuli. j speech hear disord. 1964 feb;29:23-35. doi: 10.1044/jshd.2901.23. pmid: 14122665.," *J Speech Hear Disord.*, 1964. [Online]. Available: https://pubmed.ncbi.nlm.nih.gov/14122665/ (visited on 03/19/2021).

[43] J. D. Hood, "The principles and practice of bone conduction audiometry: A review of the present position. laryngoscope. 1960 sep;70:1211-28. doi: 10.1288/00005537-196009000-00001. pmid: 13715685.," *Laryngoscope.*, 1960. [Online]. Available: https://pubmed.ncbi.nlm.nih.gov/13715685/ (visited on 03/19/2021).

[44] O. Dyrlund and N. Bisgaard, "Acoustic feedback margin improvements in hearing instruments using a prototype dfs (digital feedback suppression) system," *Scandinavian Audiology 1991; 20:49-53*, 1991. [Online]. Available: https://www.tandfonline.com/doi/citedby/10.3109/01050399109070790?scroll=top&needAccess=true (visited on 03/24/2021).

[45] T. Sankowsky-Rothe, M. Blau, H. Schepker, and S. Doclo, "Reciprocal measurement of acoustic feedback paths in hearing aids. j acoust soc am. 2015 oct;138(4):el399-404. doi: 10.1121/1.4933062. pmid: 26520351.," *J Acoust Soc Am.*, 2015. [Online]. Available: https://pubmed.ncbi.nlm.nih.gov/26520351/ (visited on 03/25/2021).

[46] D. K. Bustamante, T. L. Worrall, and M. J. Williamson, ""measurement and adaptive suppression of acoustic feedback in hearing aids," international conference on acoustics, speech, and signal processing„ glasgow, uk, 1989, pp. 2017-2020 vol.3, doi: 10.1109/icassp.1989.266855.," *International Conference on Acoustics, Speech, and Signal Processing„ Glasgow, UK, 1989, pp. 2017-2020 vol.3*, 1989. [Online]. Available: https://ieeexplore.ieee.org/document/266855 (visited on 03/25/2021).

[47] H. A. Snapp, K. E. Morgenstein, F. F. Telischi, and S. Angeli, "Transcranial attenuation in patients with single-sided deafness. audiol neurootol. 2016;21(4):237-243. doi: 10.1159/000447044. epub 2016 aug 17. pmid: 27529738.," *Audiol Neurootol.*, 2016. [Online]. Available: https://pubmed.ncbi.nlm.nih.gov/27529738/ (visited on 03/21/2021).

[48] J. J. Wazen, J. B. Spitzer, S. N. Ghossaini, J. N. Fayad, J. K. Niparko, K. Cox, D. E. Brackmann, and S. D. Soli, "Transcranial contralateral cochlear stimulation in unilateral deafness. otolaryngol head neck surg 2003;129:248–254.," *Otolaryngol Head Neck Surg*, 2003. [Online]. Available: https://pubmed.ncbi.nlm.nih.gov/12958575/ (visited on 03/21/2021).

[49] L.-M. Lin, S. Bowditch, M. J. Anderson, B. May, K. M. Cox, and J. K. Niparko, "Amplification in the rehabilitation of unilateral deafness: Speech in noise and directional hearing effects with bone-anchored hearing and contralateral routing of signal amplification. otol neurotol 2006;27:172–182.," *Otol Neurotol*, 2006. [Online]. Available: https://pubmed.ncbi.nlm.nih.gov/16436986/ (visited on 03/21/2021).

[50] M. K.S. Hol, A. J. Bosman, A. F.M. Snik, E. A.M. Mylanus, and C. W.R.J. Cremers, "Bone-anchored hearing aid in unilateral inner ear deafness: A study of 20 patients. audiol neurootol 2004;9:274–281," *Audiol Neurootol*, 2004. [Online]. Available: https://pubmed.ncbi.nlm.nih.gov/15316200/ (visited on 03/22/2021).

[51] C. Rigato, S. Reinfeldt, B. Håkansson, K. Johan Fredén Jansson, E. Renvall, and M. Eeg-Olofsson, "Effect of transducer attachment on vibration transmission and transcranial attenuation for direct drive bone conduction stimulation. hear res. 2019 sep 15;381:107763. doi: 10.1016/j.heares.2019.06.006. epub 2019 jul 12. pmid: 31387072.," *Hear Res.*, 2019. [Online]. Available: https://pubmed.ncbi.nlm.nih.gov/31387072/ (visited on 03/22/2021).

[52] A. R.Mackey, W. E. Hodgetts, and S. A. Small, "Maturation of bone-conduction transcranial and forehead attenuation using a measure of sound pressure in the ear canal. int j audiol. 2018 apr;57(4):283-290. doi: 10.1080/14992027.2017.1410585. epub 2017 dec 14. pmid: 29241372.," *Int J Audiol.*, 2018. [Online]. Available: https://pubmed.ncbi.nlm.nih.gov/29241372/ (visited on 03/23/2021).

[53] J. Li, L. Ren, T. Wu, D. Yin, P. Dai, L. Chen, and T. Zhang, "Experimental and numerical studies on vibration modes and transcranial attenuation characteristics in unilateral bone conduction hearing, shock and vibration, vol. 2020, article id 4962098, 1," *Shock and Vibration*, 2020. [Online]. Available: https://www.hindawi.com/journals/sv/2020/4962098/ (visited on 03/28/2021).

[54] T. Sankowsky-Rothe, H. Schepker, S. Doclo, and M. Blau, "Acoustic feedback path modeling for hearing aids: Comparison of physical position based and position independent models. j acoust soc am. 2020 jan;147(1):85. doi: 10.1121/10.0000509. pmid: 32006989.," *J Acoust Soc Am.*, 2020. [Online]. Available: https://pubmed.ncbi.nlm.nih.gov/32006989/ (visited on 03/27/2021).

[55] N. Kim, Y. Chang, and S. Stenfelt, "A three-dimensional finite-element model of a human dry skull for /bone-conduction hearing. biomed res int. 2014;2014:519429. doi: 10.1155/2014/519429. epub 2014 aug 27. pmid: 25243148; pmcid: Pmc4160632.," *Biomed Res Int.*, 2014. [Online]. Available: https://pubmed.ncbi.nlm.nih.gov/25243148/ (visited on 04/01/2021).

[56] Y. Chang, N. Kim, and S. Stenfelt, "The development of a whole-head human finite-element model for simulation of the transmission of bone-conducted sound. j acoust soc am. 2016 sep;140(3):1635. doi: 10.1121/1.4962443. pmid: 27914383.," *J Acoust Soc Am.*, 2016. [Online]. Available: https://pubmed.ncbi.nlm.nih.gov/27914383/ (visited on 04/01/2021).

[57] Y. Chang, N. Kim, and S. Stenfelt, "Simulation of the power transmission of bone-conducted sound in a finite-element model of the human head. biomech model mechanobiol. 2018 dec;17(6):1741-1755. doi: 10.1007/s10237-018-1053-4. epub 2018 jul 17. pmid: 30019294.," *Biomech Model Mechanobiol.*, 2018. [Online]. Available: https://pubmed.ncbi.nlm.nih.gov/30019294/ (visited on 04/01/2021).

[58] Y. Chang and S. Stenfelt, "Characteristics of bone-conduction devices simulated in a finite-element model of a whole human head. trends hear. 2019 jan-dec;23:23312165198-36053. doi: 10.1177/2331216519836053. pmid: 30880644; pmcid: Pmc6423684.," *Trends Hear.*, 2019. [Online]. Available: https://pubmed.ncbi.nlm.nih.gov/30880644/ (visited on 04/02/2021).

[59] A. Brown, J. Walters, Y. Zhang, M. Saadatfar, J. Escobedo-Diaz, and P. Hazell, "The mechanical response of commercially available bone simulants for quasi-static and dynamic loading. j mech behav biomed mater. 2019 feb;90:404-416. doi: 10.1016/j.jmbbm.2018.10.032. epub 2018 oct 30. pmid: 30445367.," *Journal of the Mechanical Behavior of Biomedical Materials*, 2019. [Online]. Available: https://pubmed.ncbi.nlm.nih.gov/30445367/ (visited on 12/07/2020).

[60] T. Plaisted and J. Gardner, "Development of cranial bone surrogate structures using stereolithographic additive manufacturing," *US Army Research Laboratory*, 2017. [Online]. Available: https://www.semanticscholar.org/paper/Development-of-Cranial-Bone-Surrogate-Structures-Plaisted-Gardner/b216999804aad35d37-c2e78ce40cce8ea247ebc4#references (visited on 12/07/2020).

[61] L. Falland-Cheung, J. Waddell, K. Chun Li, D. Tong, and P. Brunton, "Investigation of the elastic modulus, tensile and flexural strength of five skull simulant materials for impact testing of a forensic skin/skull/brain model. j mech behav biomed mater. 2017 apr;68:303-307. doi: 10.1016/j.jmbbm.2017.02.023. epub 2017 feb 20. pmid: 28236695," *Journal of the Mechanical Behavior of Biomedical Materials*, 2017. [Online]. Available: https://pubmed.ncbi.nlm.nih.gov/28236695/ (visited on 12/12/2020).

[62] J. Roberts, A. Merkle, C. Carneal, L. Voo, M. Johannes, J. Paulson, S. Tankard, and O. Uy, "Development of a human cranial bone surrogate for impact studies. front bioeng biotechnol. 2013 oct 24;1:13. doi: 10.3389/fbioe.2013.00013. pmid: 25023222; pmcid: Pmc4090900.," *Frontiers in Bioengineering and Biotechnology*, 2013. [Online]. Available: https://pubmed.ncbi.nlm.nih.gov/25023222/ (visited on 12/12/2020).

[63] A. Forte, S. Galvan, F. Manieri, F. Baena, and D. Dini, "A composite hydrogel for brain tissue phantoms," *Elsevier - Materials and Design*, 2016. [Online]. Available: https://www.researchgate.net/publication/308344339_A_composite_hydrogel_for_brain_tissue_phantoms (visited on 12/17/2020).

[64] Z. Tan, J. Ewen, A. Forte, S. Galvan, E. De Momi, F. Baena, and D. Dini, "What does a brain feel like?, journal of chemical education 2020 97 (11), 4078-4083, doi: 10.1021/acs.jchemed.0c00957," *Journal of Chemical Education*, 2020. [Online]. Available: https://pubs.acs.org/doi/10.1021/acs.jchemed.0c00957 (visited on 12/18/2020).

[65] A. Leibinger, A. Forte, Z. Tan, M. Oldfield, F. Beyrau, D. Dini, and Y. B. F. Rodriguez, "Soft tissue phantoms for realistic needle insertion: A comparative study. ann biomed eng. 2016 aug;44(8):2442-2452. doi: 10.1007/s10439-015-1523-0. epub 2015 dec 14. erratum in: Ann biomed eng. 2016 oct 4;: Pmid: 26666228; pmcid: Pmc4937066.," *Annals of Biomedical Engineering*, 2015. [Online]. Available: https://pubmed.ncbi.nlm.nih.gov/26666228/ (visited on 12/29/2020).

[66] A. Chanda, C. Callaway, C. Clifton, and V. Unnikrishnan, "Biofidelic human brain tissue surrogates," *Mechanics of Advanced Materials and Structure*, 2016. [Online]. Available: https://www.tandfonline.com/doi/full/10.1080/15376494.2016.1143749?scroll=top&needAccess=true (visited on 12/29/2020).

[67] D. Singh, S. Boakye-Yiadom, and D. Cronin, "Comparison of porcine brain mechanical properties to potential tissue simulant materials in quasi-static and sinusoidal compression. j biomech. 2019 jul 19;92:84-91. doi: 10.1016/j.jbiomech.2019.05.033. epub 2019 may 24. pmid: 31151795.," *Journal of Biomechanics*, 2019. [Online]. Available: https://pubmed.ncbi.nlm.nih.gov/31151795/ (visited on 12/29/2020).

[68] A. Dabrowska, G. Rotaru, F. Spano, C. Affolter, G. Fortunato, S. Lehmann, S. Derler, N. Spencer, and R. Rossi, "A water-responsive, gelatine-based human skin model, volume 113, september 2017, pages 316-322," *Tribology International*, 2017. [Online]. Available: https://www.sciencedirect.com/science/article/pii/S0301679X17300361 (visited on 01/01/2021).

[69] A. Chanda, "Biomechanical modeling of human skin tissue surrogates. biomimetics (basel). 2018 jul 23;3(3):18. doi: 10.3390/biomimetics3030018. pmid: 31105240; pmcid: Pmc6352690.," *Biomimetics*, 2018. [Online]. Available: https://pubmed.ncbi.nlm.nih.gov/31105240/ (visited on 01/02/2021).

[70] A. Dąbrowska, G. Rotaru, S. Derler, F. Spano, M. Camenzind, S. Annaheim, R. Stämpfli, M. Schmid, and R. Rossi, "Materials used to simulate physical properties of human skin. skin res technol. 2016 feb;22(1):3-14. doi: 10.1111/srt.12235. epub 2015 jun 12. pmid: 26096898.," *Skin Research and Technology*, 2016. [Online]. Available: https://pubmed.ncbi.nlm.nih.gov/26096898/ (visited on 01/03/2020).

[71] K. Whittle, J. Kieser, I. Ichim, M. Swain, N. Waddell, V. Livingstone, and M. Taylor, "The biomechanical modelling of non-ballistic skin wounding: Blunt-force injury. forensic sci med pathol. 2008;4(1):33-9. doi: 10.1007/s12024-007-0029-y. epub

2007 aug 15. pmid: 19291467.," *Forensic Sci Med Pathol.*, 2008. [Online]. Available: https://pubmed.ncbi.nlm.nih.gov/19291467/ (visited on 01/03/2020).

[72] *Humimic - synthetic gelatin 5*, https://humimic.com/product/gelatin-5-medical-gel-by-the-pound/, Accessed: 2021-04-04.

[73] *Smooth-on inc - flexfoam-it series*, https://www.smooth-on.com/product-line/flexfoam-it/, Accessed: 2021-04-04.

[74] *Forensic source - permagel*, https://forensicssource.com/products/permagel-large-test-block-1005752, Accessed: 2021-04-04.

[75] S. Stenfelt, B. Hakansson, and A. Tjellstrom, "
vibration characteristics of bone conducted sound in vitro," journal of the acoustical society of america, vol. 107, pp. 422–431, 2000.," *Journal of the Acoustical Society of America*, 2000. [Online]. Available: https://pubmed.ncbi.nlm.nih.gov/10641651/ (visited on 04/13/2021).

[76] S. Stenfelt and R. Goode, ""transmission properties of bone conducted sound: Measurements in cadaver heads," journal of the acoustical society of america, vol. 118, pp. 2373–2391, 2005.," *Journal of the Acoustical Society of America*, 2005. [Online]. Available: https://pubmed.ncbi.nlm.nih.gov/16266160/ (visited on 04/13/2021).